Palladium core superparamagnetic iron oxide nanoparticles for imaged – guided thermotherapy

Comparison between synthesized and commercial nanoparticles

Master Thesis

By

Anestis Nakas

Master of Science

in Biomedical Engineering

Delft University of Technology

Supervisor: Associate Professor Antonia Denkova
Second Supervisor: Associate Professor Kristina Djanashvili

TU Delft

Palladium core superparamagnetic iron oxide nanoparticles for imaged – guided thermotherapy

Comparison between synthesized and commercial nanoparticles

By

Anestis Nakas

in partial fulfilment of the requirements for the degree of

Master of Science
in Biomedical Engineering

at the Delft University of Technology,
to be defended publicly on Wednesday December 16, 2020 at 10:00 AM.

Supervisor:	Associate Professor Antonia Denkova
Thesis committee:	Associate Professor Antonia Denkova Associate Professor Kristina Djanashvili Associate Professor Frans Vos

This thesis is confidential and cannot be made public until December 16, 2020.

Contents

Contents 3
Abstract 5
Acknowledgements 5
1 Introduction 6
2 Theory 8
2.1. Superparamagnetism 8
2.2. Heating mechanisms in Magnetic Nanoparticle Thermotherapy 8
2.2.1. Néel relaxation losses 8
2.2.2. Brownian relaxation losses 9
2.3. Quantification of the generated heat 9
2.4. SLP calculation methods 10
2.4.1. Initial Slope Method 10
2.4.2. Modified Law of Cooling 10
2.5. SPIONs for thermotherapy 11
2.5.1. SPIONs size 11
2.5.2. SPIONs anisotropy 11
2.5.3. SPION coating 12
2.5.4. Monodispersity 12
2.5.5. Aggregation state 13
2.5.6. Viscosity of surrounding fluid 13
2.5.7. Magnitude and Frequency of AMF 13
2.6. Magnetic Resonance Imaging (MRI) 14
2.6.1. Spin echo sequence 16
2.6.2. Gradient echo sequence 16
2.7. Contrast agents in MRI 17
2.7.1. Quantification of the contrast enhancement 17
2.7.2. T1 contrast agents 17
2.7.3. T2 contrast agents 18
2.8. SPIONs as T2 CAs 18
2.8.1. SPIONs saturation magnetization 18
2.8.2. SPIONs size 19
2.8.3. SPIONs composition 19
2.8.4. SPIONs shape 19
2.8.5. SPIONs coating 20
2.8.6. SPIONs aggregation state 20
3 Materials and Methods 22
3.1. Pd – SPIONs synthesis and functionalization 22
3.2. Structural and Magnetic Characterization of Oleic Acid/Oleylamine coated Pd – SPIONs 22
3.3. Structural and Magnetic Characterization of DMSA and DSPE – PEG$_{2000}$ COOH coated Pd – SPIONs 23
3.4. Calometric measurements 24
3.4.1. Calometric measurements in hexane 24
3.4.2. Calometric measurements in water 25
3.5. SLP calculation during calometric experiments 25
3.6. Relaxivity measurements 26
3.7. MRI and CT studies 27
4 Results and Discussion 29
4.1. Structural Characterization for the Pd - SPIONs solubilized in hexane 29
4.2. Magnetic Characterization for the Pd – SPIONs dispersed in hexane 32
4.3. Structural Characterization for the Pd - SPIONs in water 34

4.4. Magnetic Characterization for the Pd - SPIONs coated with DSPE – PEG$_{2000}$ COOH and commercial particles coated with DMSA 36
4.5. Calometric measurements 38
4.6. Parameters affecting the heating performance of Pd – SPIONs dispersed in hexane 40
4.6.1. Size 40
4.6.2. Polydispersity 40
4.6.3. Aggregation state 40
4.6.4. Morphology 41
4.6.5. Magnetization 41
4.7. Heating performance of Pd - SPIONs dispersed in water 42
4.8. Contrast enhancing performance of Pd - SPIONs dispersed in water 46
4.9. MRI and CT studies with commercial SPIONs 47
5 Conclusion 51
6 Future Research 52
Bibliography 53
Appendix I 57

Abstract

Heat in thermal therapy can be produced by exposing superparamagnetic iron oxide nanoparticles (SPIONs) to alternating magnetic fields in order to treat cancer. In addition, Magnetic Resonace Imaging (MRI) uses SPIONs as T_2 contrasts agents for diagnostic purposes. This attribute gives SPIONs potential to be used as theranostic agents in MRI – guided thermotherapy in order to visualize the concentration of the particles within the tumour and monitor the effect of the treatment. The performance of SPIONs as heating and contrast agents is highly dependent on their physical and magnetic properties. In this study, six different samples of palladium core superparamagnetic iron oxide nanoparticles (Pd – SPIONs), a formulation that has not been found in literature until today, synthesized at the Reactor Institute Delft were provided. The goal of this MSc Thesis was to determine the structural and magnetic particle parameters of Pd - SPIONs that were related with optimal heating and contrast enhancing performance in thermotherapy and MRI, respectively. For this purpose, all samples were fully characterized and their performances as heating and MRI contrast agents were investigated and compared along with commercial nanoparticles. In addition, MRI phantom and CT studies were performed using the commercial nanoparticles in order to determine whether quantification of different concentrations was possible.

Acknowledgements

I would like express my sincere gratitude to Associate Professors Antonia Denkova and Kristina Djanashvili for giving the opportunity to work in a friendly, enthusiastic and multicultural research group. Their continuous support and motivation throughout this thesis granted me with immense knowledge and skills. Also, special thanks to PhD candidates Rogier Van Oossanen and Alexandra Maier for their supervision and encouragement throughout my research work.

1 Introduction

Breast cancer is a disease that affects thousands of women every year, with the Netherlands being the third among 185 countries with the highest breast cancer rate for 2018[1]. Many treatment methods exist showing promising results among which are surgery, radiation therapy, chemotherapy and thermal therapy[2–9], as illustrated in Fig. 1. Combinations of different treating modalities are usually used. In many cases the treatment protocol for breast cancer treatment involves surgery accompanied by radiation therapy lasting over few months[9]. Even though this strategy prolongs the survival of patients[10], it suffers from the huge treatment burden of surgery and long – term side effects that might result from radiation therapy[11]. Thus, an alternative minimally invasive treatment protocol with less burden and reduced side effects is needed. To this regard, the Applied Radiation Isotope (ARI) Group of the Reactor Institute Delft (RID) has proposed a new method, were intratumorally injected ^{103}Pd – core superparamagnetic iron oxide nanoparticles (^{103}Pd – SPIONs) enable Thermal Ablation (TA) and Brachytherapy (BTh) as well as real – time monitoring of the treatment in order to ensure a minimally invasive, image - guided treatment with minimal side effects.

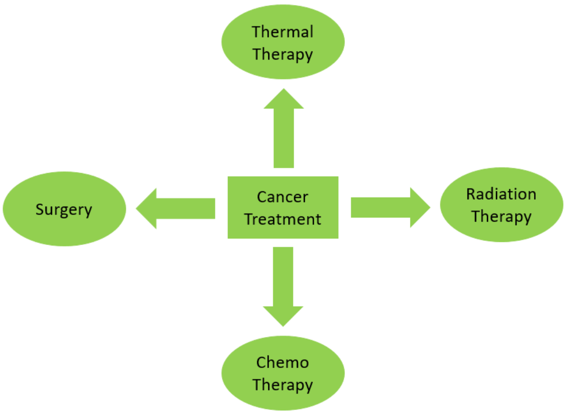

Figure 1: Most commonly used modalities for cancer treatment

Thermal therapy involves Hyperthermia or Thermal Ablation (TA). Hyperthermia can be used as an adjunct to Radiation Therapy[3–8]. During Hyperthermia treatment tumours are subjected to temperatures up to 42 °C[4,7]. This increases the oxygen flow within the tumour cells, a fact that enhances the performance of Radiation Therapy. In TA temperatures above 50 °C are reached[4,7]. This modality uses lethal doses of heat that induce immediate cancer cell death via apoptosis and/or necrosis and thus ablate tumours[4,5].

Heat in thermal therapy can be delivered in tissue via various methods: (a) focusing ultrasound waves into a focal point, (b) using microwaves, (c) exposing magnetic nanoparticles (MNPs) to alternating magnetic fields (AMFs), etc.[4,5,7,8]. Regarding the latter method, the electromagnetic energy from the AMF is converted to heat[4–8] which can be used for cancer treatment. This method was first proposed by Gilchrist et al.[12] in 1957, during which MNPs were injected into tumour tissue and subjected to alternating magnetic fields (AMFs) in order to treat lymph node cancer. To this notion, it can be assumed that MNPs capable of producing temperatures above 50 °C under AMF exposure, would enable TA and therefore ablate tumour tissue in a similar manner to surgery, but in a minimally invasive way without burden.

However, even after the tumour is ablated, remaining cancer cells can still be present. This is the reason why surgery, in the first place, is accompanied by radiation therapy, i.e. radiation ensures that any cancer cells left behind are killed, a protocol though that can lead to long – term side effects[11]. Therefore, in the case of the TA treatment with MNPs, it is important that all the remaining cancer cells are eliminated. For this purpose, the proposed particles consist of a radioactive ^{103}Pd core that can enable low energy brachytherapy which can kill the remaining cancer cells. The whole treatment is performed once since after injection the nanoparticles will be eventually removed from the tissue by the immune system. Therefore, reduced long – term side effects would be expected. The ^{103}Pd isotope was chosen since it has found success in clinic in previous trials[13]. The low radiation energy emitted can cause the irradiation of the tumour while spearing healthy tissue.

A schematic representation of the ^{103}Pd – SPIONs can be seen in Fig. 2. The particles consist of a ^{103}Pd core, surrounded by a superparamagnetic iron oxide middle shell. The middle shell would enable the TA under AMF exposure, while the ^{103}Pd core would deliver the brachytherapy dose. The particles are coated with a hydrophilic surfactant to ensure colloidal stability, reduce aggregation and avoid detection from the immune system. The most commonly used iron oxides are magnetite (Fe_3O_4) and maghemite (γ-Fe_2O_3), because of their high biocompatibility and negligible toxicity[4,6,8].

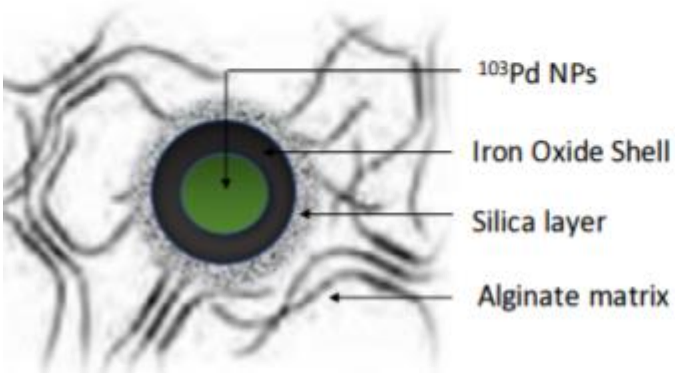

Figure 2: Schematic representation of the ^{103}Pd - SPIONs

In addition, SPIONs have been throughoutly used in static magnetic fields as T_2 contrast agents in Magnetic Resonance Imaging (MRI) for diagnostic purposes[14]. This attribute gives SPIONs potential to be used as theranostic agents in MRI – guided thermotherapy in order to visualize the concentration of the particles within the tumour and monitor the effect of the treatment.

Taking all the above into account, ^{103}Pd – SPIONs enable an MRI – guided thermo – brachytherapy approach for breast cancer treatment that has not been presented before in literature.

In this study multiple SPION samples with non – radioactive Pd core (Pd – SPIONs) synthesized at the RID were provided along with commercial SPION nanoparticles (Hypermag® by NanoTherics[15]), since focus was placed on the investigation of nanoparticle performance in thermal therapy and MRI and not in BTh. Based on literature, the performance of SPIONs as heating and T_2 contrast agents, respectively is highly determined by their physical and magnetic properties. Thus, the goal of this thesis was to evaluate the physical and magnetic particle parameters that were related with optimal heating and contrast enhancing performance for the Pd – SPIONs, since such formulation does not exist in literature up to this point. All samples were fully characterized and their performances as heating and MRI contrast agents were investigated and compared. The performance of the commercial particles was also accounted in the comparison. In addition, MRI phantom and CT studies were performed using the commercial nanoparticles in order to determine whether quantification of different concentrations was possible. Before discussing any of the experimental methods and results of this study, a theoretical background discussing how SPION properties affect their heating and contrast enhancing performance is first presented.

2 Theory

2.1. Superparamagnetism

Superparamagnetism is a form of magnetism that appears when ferromagnetic or ferrimagnetic materials become smaller than a critical size. For magnetite (Fe_3O_4) and maghemite ($\gamma - Fe_2O_3$) this size is 25 nm. In this state, thermal fluctuations cause the atomic magnetic moments to flip directions randomly. The time between two flips is called Néel relaxation time (t_N). In the absence of an external magnetic field the magnetization is zero on average. When an external magnetic field is applied, the magnetic moments orient parallel to the field, similar to a paramagnet. The net magnetic moment will be greater than a paramagnet, which justifies the name 'superparamagnet'[4–7,16,17].

Temperature also plays an important role. There is a critical temperature known as blocking temperature (T_B), above which materials falling into the superparamagnetic regime show superparamagnetic behavior, whereas below T_B the thermal energy is not high enough to cause the random flipping of the magnetic moments and the material is known to be in a blocked state [5,17].

2.2. Heating mechanisms in Magnetic Nanoparticle Thermotherapy

The heating mechanisms of SPIONs under AMF exposure are described by the Linear Response Theory (LRT) developed by Rosensweig[18]. According to this model there are two different heating mechanisms, under which the AMF energy is converted to heat: (a) Néel relaxation losses and (b) Brownian relaxation losses. The heat dissipation is given by the relation:

$$P = \chi_0 \mu_0 \pi H_0^2 \frac{2\pi f^2 \tau}{1 + (2\pi f \tau)^2} \quad (1)$$

where χ_0 is the initial susceptibility, μ_0 is the permeability of free space, H_0 is the AMF field amplitude, f is the frequency of the measurement, and τ is the effective relaxation time[5,6,19,20]. The relaxation time is given as:

$$\frac{1}{\tau} = \frac{1}{\tau_B} + \frac{1}{\tau_N} \quad (2)$$

where τ_B the characteristic Brownian relaxation time and τ_N the characteristic Néel relaxation time.

2.2.1. Néel relaxation losses

During Néel relaxation, the interaction of AMFs with SPIONs causes the rotation of the atomic magnetic moments with respect to the nanoparticles (Fig. 3A). The characteristic Néel relaxation time is given by the relation:

$$\tau_N = \tau_0 e^{\frac{KV}{k_B T}} \quad (3)$$

where τ_0 is the attempt time in seconds (characteristic of a material), K is the effective anisotropy constant, V is the SPION volume, k_B is the Boltzmann constant and T is the absolute temperature[4–7,21].
From equation (3) can be seen that Néel relaxation depends on the effective anisotropy constant K. A SPION's anisotropy dictates a fixed orientation to the particle's net magnetic moment, since it is more energetically favourable for the magnetization to align in the direction its anisotropy commands it, rather than in another one. When a particle is subjected to AMFs, its net magnetization is constantly aligning in the

direction of the applied field, against the direction its anisotropy dictates it to orient. This produces magnetic friction, which generates heat in return [4–7,21].

2.2.2. Brownian relaxation losses

During Brownian relaxation, when an AMF is applied SPIONs rotate as a whole (Fig. 3B). The characteristic Brownian relaxation time is:

$$\tau_B = \frac{3\eta V_H}{k_B T} \quad (4)$$

, where η is the viscosity and V_H is the hydrodynamic diameter of a SPION [4–7,21].

From equation (4) it can be seen that the viscosity η of the fluid the SPIONs are embedded in greatly influences the Brownian relaxation time. When subjected to AMFs, SPIONs physically rotate in a rapid manner and align with the direction of the applied field. Due to the viscosity of the surrounding fluid, SPIONs' rotation causes friction and heat is generated [4–7,21].

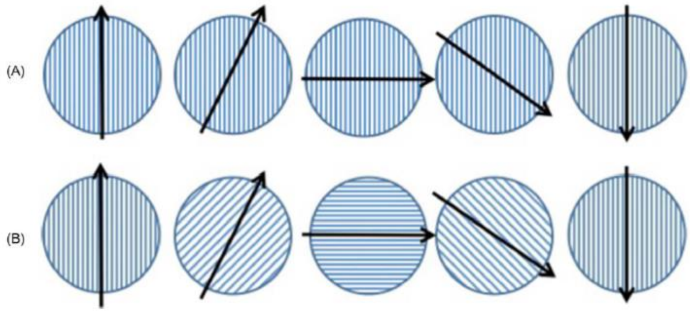

Figure 3: Schematic of (A) Neel and (B) Brownian motion[7]

2.3. Quantification of the generated heat

The amount of heat generated by SPIONs under the influence of the AMFs is measured via the Specific Loss Power (SLP):

$$SLP = \frac{m_s}{m_n} C_p \frac{\Delta T}{\Delta t} \quad (5)$$

, where C_p is the specific heat of the colloid, m_s is the mass of the solvent in mg, m_n is the mass of the SPIONs in mg and $\Delta T/\Delta t$ is the measured temperature increase over time. In order for the temperature to reach 50 °C, high SLP values are needed[4–7,21,22].

The SLP value depends strongly on the frequency and magnitude of the applied alternating field. In order to compare results taken from different experimental setups, a normalized version of SLP is used, named Intrinsic Loss Power (ILP):

$$ILP = \frac{SLP}{H^2 f} \quad (6)$$

, where H is the magnitude of the AMF and f its frequency[21,22].

2.4. SLP calculation methods

The SLP is ideally calculated under adiabatic conditions during which heat transfer from the heating sample to the environment is absent[19,23–26]. In such conditions all the heat produced by the particles under AMF exposure is invested in the temperature rise of the sample solution which increases the accuracy of SLP calculations. Recording of the temperature profile over time during AMF exposure would therefore yield a linear heating curve as can be seen in Fig. 4. However, such setups are difficult to build and the measurements are time consuming, which is why most of the up to date thermotherapy experiments are performed under non – adiabatic conditions, during which heat losses to the surrounding space occur as soon as the sample's temperature becomes higher than the environmental one[19,23–26]. All this external heat transfer results in an exponential heating curve, curving downwards as can be seen in Fig. 4. Thus, non – adiabatic setups can lead to inaccuracies in the calculation of SLP if the external heat losses are not taken into account[19,23–27].

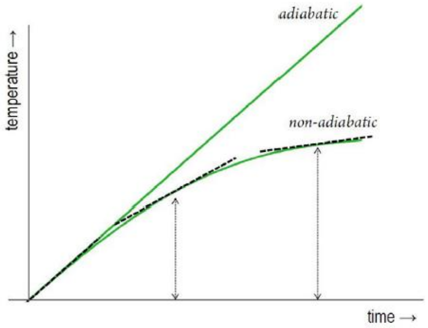

Figure 4: Temperature profiles over time taken from calometric measurement under adiabatic and non – adiabatic conditions[26]

It is important that the losses are quantified and included in the calculation of the SLP. To this regard, two different methods can be implemented: (a) the initial slope method and (b) the modified law of cooling[19,23–27].

2.4.1. Initial Slope Method

The initial slope method has widespread application in thermotherapy studies[19]. Assuming that at the very early moments of the heating process heat losses are negligible, since the heating sample is at its baseline temperature, this method approximates the temperature slope at the very first seconds of heating:

$$SLP = \frac{m_s}{m_n} C_p \left.\frac{\Delta T}{\Delta t}\right|_{t\to 0} \qquad (7)$$

This method, however, can be sensitive to inaccuracies given the fact that external heat losses could be significant even at the start of the heating process. This could happen for example in cases that the sample's temperature has increased enough to be higher than the baseline temperature[19,23–27].

2.4.2. Modified Law of Cooling

The modified law of cooling excludes external heat losses and extracts the actual temperature rise caused by the nanoparticles[24]. By exponentially fitting the cooling stage of the curve (after removal of the AMF exposure) the cooling constant (k) and the thermal losses to the environment can be estimated. The actual heat generated by the particles is the sum of the part absorbed by the sample solution and the external losses:

$$\frac{dT'}{dt} = \frac{dT}{dt} + k(T - T_{out}) \qquad (8)$$

, where $\frac{dT'}{dt}$ is the corrected slope, $\frac{dT}{dt}$ is the slope of the heating curve calculated by the initial slope method, k is the cooling constant, T is the temperature during the heating process and T_{out} is the temperature of the environment. The corrected slope is used for the SLP estimation. By implementing this method a non – adiabatic heating curve is transformed to an adiabatic one[19,23,24,27].

Makridis et al.[19] compared different SLP calculation methods among which were the initial slope method and the modified law of cooling. They resulted that the latter method yielded the most credible SLP values.

2.5. SPIONs for thermotherapy

The heating performance of SPIONs is highly dependent on many parameters. Parameters of key importance in heat generation are: (a) size, (b) anisotropy, (c) shape, (d) coating, (e) sample monodispersity as well as (f) aggregation state, (g) viscosity of surrounding fluid, (h) magnitude and frequency of the applied AMF.

2.5.1. SPIONs size

According to the LRT model, SLP values increase with size up to a certain value[28–32]. There is an optimum size which is related with enhanced heating performance and if that size is exceeded the SLP values drop (Fig. 5). Vreeland et al.[33] found in their work that the optimum size of SPIONs related with the highest SLP value was 22 nm.

Volume increases with size and in return this leads to higher temperatures and SLP values. This is because in larger sizes the surface to volume ratio of the particles decreases and spin canting effects become less significant. Thus, the magnetization of SPIONs is higher and since according to the LRT model there is a linear relation between SLP and magnetization, it is concluded that larger particles lead to higher SLPs. However, sizes larger than the superparamagnetic regime limit lead to ferromagnetic particles, which are undesirable because of their aggregation tendencies. At this state the heating mechanisms cannot be described by the LRT model and hysteresis heating is pronounced. When particles lie in the superparamagnetic regime, their lack of remanent magnetization makes them more stable than ferromagnetic ones.

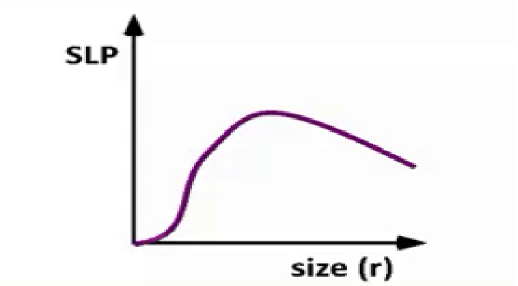

Figure 5: SLP as a function of size. There an optimum size that is related with enchanced heating rates[19]

2.5.2. SPIONs anisotropy

According to the LRT model, one of the main SPIONs heating mechanisms is Néel relaxation. From equation (3) can be seen that the Néel characteristic time depends on the effective anisotropy constant *K*. The effective anisotropy constant involves all contributions to anisotropy[5]:

- Magnetocrystalline anisotropy – occurs when crystal structure dictates the magnetic moment orientation
- Shape anisotropy – occurs when shape dictates the orientation according to the major axes
- Surface anisotropy - occurs due to changes in composition at crystal boundaries

Magnetocrystalline anisotropy is related to the composition of SPIONs. Anisotropy can be improved by doping SPIONs with metals having large magnetic moments, like gadolinium (Gd) or cobalt (Co). This translates into replacing a Fe atom with a Gd or Co atom, which increases anisotropy and in return leads to higher temperatures and SLP values[22,34]. Lee et al.[35] shown that manganese or cobalt ferrites lead to higher heating rates than magnetite particles of identical sizes (Fig. 6).

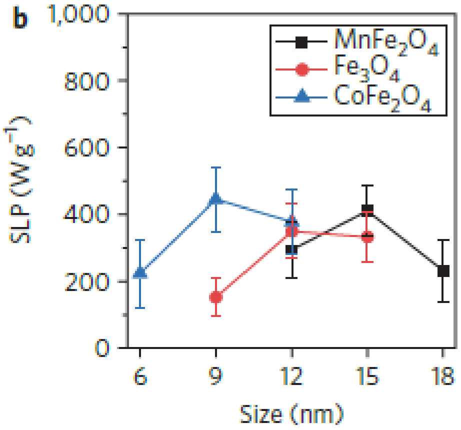

Figure 6: SLP values for different ferrites of identical sizes[35]

Shape anisotropy is another form of anisotropy that affects the heating performance of SPIONs. In general it is known that cubic SPIONs present higher shape anisotropy than spherical SPIONs[29] and thus higher effective anisotropy, which translates to higher SLP values in return. Cubic SPIONs present lower surface anisotropy when compared to spherical SPIONs, because spheres have more curved surface and therefore spin canting is more pronounced. Spin canting leads to lower magnetization and thus poorer heating performance. Bauer et al.[36] compared the heating performance of cubic and spherical SPIONs with the same magnetic volumes and observed higher SLP values for the cubic particles.

2.5.3. SPION coating

Coating is another parameter that influences the heating performance of SPIONs. Even though SPIONs do not magnetically attract each other due to lack of remanent magnetization, they still show tendencies for agglomeration. Nanoparticles in general are characterized by a high surface – to – volume ratio because of their very small sizes. Forces like surface tension and Van der Waals forces cause the aggregation of particles. The agglomeration can lead to uneven heat distribution within the tumour, which hinders the efficacy of the treatment. In order to prevent aggregation, nanoparticles are coated. The most used coating agents are polymers like dextran or polyetheleneglocol PEG[6,37].

It has been shown that the coating can affect the magnetization of SPIONs[38,39]. Increased coating thickness might interact with the surface atoms of the particles and form a magnetically dead layer and thus cause significant spin canting, which reduces the magnetization. SLP values depend on the magnetization, therefore a decrease of the latter results in less heat generated.

2.5.4. Monodispersity

Monodispersity is another property that affects the heating performance of SPIONs. In section 2.4.1 was shown that there is a critical size that causes enhanced SLP values. Sizes above or below that critical size result in lower heating rates. Thus, increased polydispersity can decrease the heating capability of a sample[28].

2.5.5. Aggregation state

As mentioned previously, nanoparticles have the tendency to agglomerate. Depending on the agglomeration state, the heating performance will either be improved or decreased. When the aggregation is controlled so that it results in ordered structures like chains, the magnetization increases due to the unidirectional magnetization orientation. This will in turn lead to an improved heating performance[29]. Controversy, when particles stabilize in solution as agglomerated suspensions resulting in heavy sedimentation, the heating efficiency is lowered[29].

2.5.6. Viscosity of surrounding fluid

From equation (4) can be seen that the Brownian relaxation characteristic time depends on the viscosity η of the fluid. Due to viscosity, rotational friction occurs when nanoparticles are subjected to AMFs and heat is generated. Higher viscosity makes that particles rotate with greater difficulty and thus less heat is generated and therefore lower SLP values are obtained[6].

2.5.7. Magnitude and Frequency of AMF

The generated heat depends on the frequency and amplitude of the applied field. From equation (1) can be seen that $P \propto H_0^2$ and $P \propto \frac{f^2}{1+f^2}$. The higher the frequency and magnitude, the higher the obtained SLP values. However, very high frequency – magnitude values are not suitable for the application of clinical thermotherapy. This is in order to avoid Joule heating resulting from eddy currents. Eddy currents appear randomly thought-out the human body, leading to non – specific heating and discomfort in patients[5,6].

2.6. Magnetic Resonance Imaging (MRI)

MRI is a non – invasive imaging modality used thoroughly in biomedical applications. In principle, a strong static magnetic field $\overrightarrow{B_0}$ is generated inside a MRI scanner, affecting the protons of hydrogen atoms in the human body. Protons can be visualized as tiny magnets undergoing two rotational motions, (a) spin motion – rotational motion around their own axis and (b) precession motion – rotation around the longitudinal axis of the applied magnetic field, as can be seen in Fig. 7b. The precession frequency is given by the formula: $\vec{\omega} = \gamma \overrightarrow{B_0}$ where γ is the gyromagnetic ratio of protons (γ = 42.58 MHz/T) and $\overrightarrow{B_0}$ is the applied magnetic field[40–43].

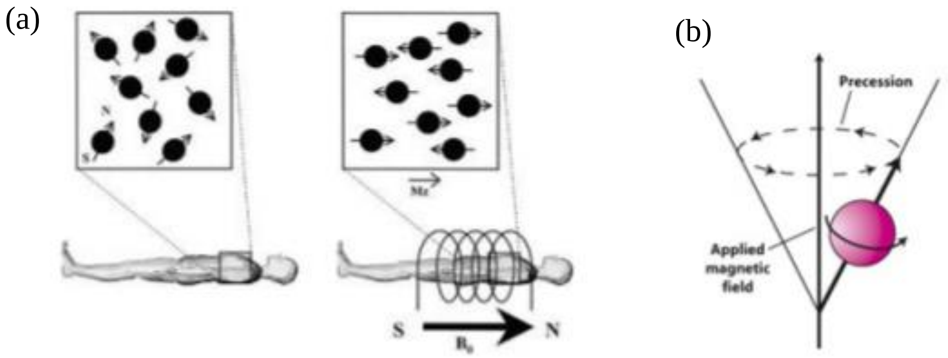

Fig. 7: (a) MRI working principle[42], (b) proton's rotational motions inside an applied magnetic field[44]

The static $\overrightarrow{B_0}$ forces all the atomic magnetic moments of hydrogen inside the human body to parallel or antiparallel precession with the field's direction (Fig.7a). According to the Boltzmann equation there are more magnetic moments parallel than antiparallel to $\overrightarrow{B_0}$, which gives rise to a net magnetization $\overrightarrow{M_0}$ in the longitudinal direction (Fig. 8a)[40–43]. A radiofrequency (RF) pulse is exerted in the perpendicular direction (Fig. 8b) forcing $\overrightarrow{M_0}$ to flip in the transversal plane in an angle called flip angle. In this state protons are in an excited state[40–43]. Once the net magnetization precesses on the transversal plane, a signal can be measured with a wire loop (Fig. 8c). The rotating magnetic moment induces an alternating current in the wire, which can be processed to a signal (Fig. 8d, 8e). This signal depends strongly in the amount of magnetization preceding in the transversal plane [40–43].

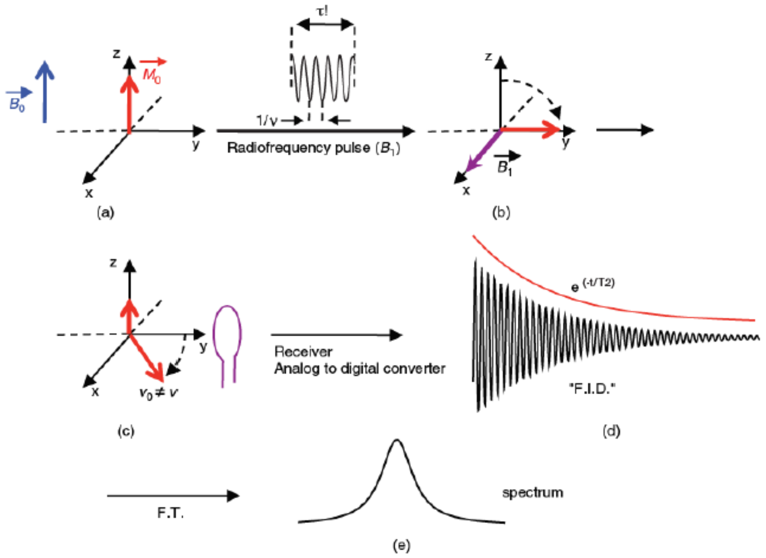

Figure 8: Signal generation during an MRI experiment[40]

When $\vec{M}_0$ arrives at the x – y plane the RF pulse is switched off. Two types of relaxation processes occur, during which the net magnetic moment returns back to the longitudinal plane, namely, T_1 and T_2 relaxations. During T_1 relaxation, there is exponential recovery of the net magnetization in the longitudinal plane over time (Fig. 9a). The relaxation is governed by the T_1 constant which gives an indication of how quickly there is recovery to 63% of the original magnetization. During T_2 relaxation, there is exponential disappearance of $\vec{M}_0$ in the transversal plane over time (Fig. 9b) This relaxation is governed by the T_2 contrast which indicates how long it takes until 37% of the original magnetization is still precessing in the transversal plane [40–43].

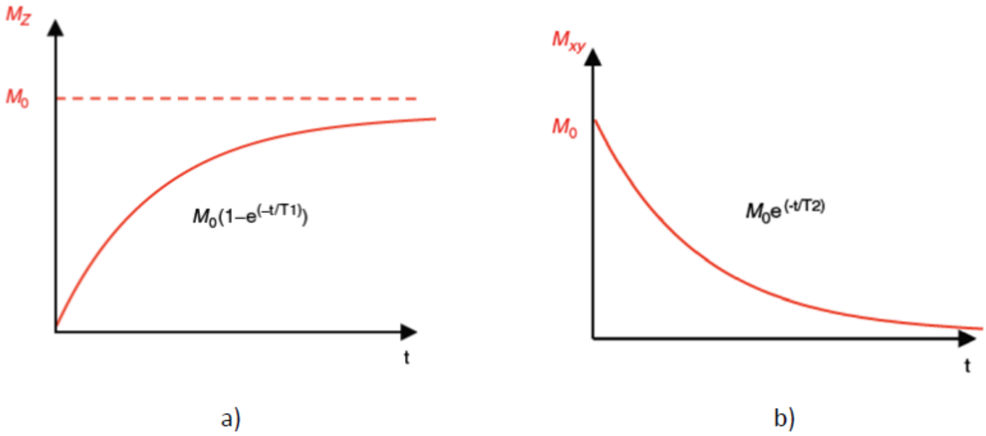

Figure 9: a) Longitudinal relaxation over time, b) transverse relaxation over time[40]

In principle $T_1 > T_2$. After the application of the RF pulse, protons are in an excited state, so they need to return to rest situation after the removal of the pulse. T_1 and T_2 relaxations both describe this process. However, the primary reason for T_2 relaxation is the dephasing of atomic spins in the transverse plane [40–43]. In more detail, the net magnetization $\vec{M}_0$ consists of atomic magnetic moments all of which undergo molecular interactions. Due to these interactions each magnetic moment precedes with a different frequency than the rest. Therefore, some spins precede faster and some slower which leads to dephasing, as can be seen in Fig. 10. Another reason for dephasing, related to field inhomogeneities is known as T_2* effects. Inside an MRI scanner when an object is submerged into a large homogeneous magnetic field (1.5T or 3T), the object itself causes field inhomogeneities within the scanner. As a result, spins rotate with different frequencies, a factor that further enhances dephasing [40–43].

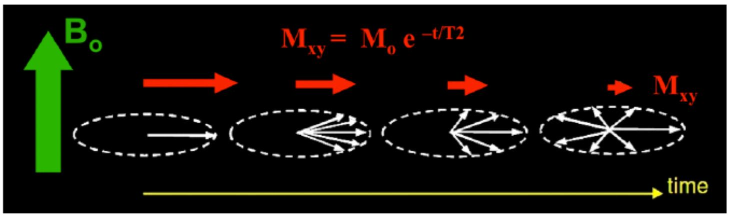

Figure 10: Dephasing of atomic magnetic moments in the transverse plane[45]

There is a crucial difference between the two effects leading to dephasing. The molecular interactions are random, therefore there is no way to compensate for this effect. Field inhomogeneities, however, can be considered static as long as the object remains in the scanner. By applying a spin echo sequence it is possible to compensate for T_2* effects[43].

2.6.1. Spin echo sequence

As mentioned previously, due to dephasing some atomic spins will precede faster than others. In a spin echo sequence, after applying the RF pulse, a second RF pulse named 180° pulse, is applied and flips the net magnetic moment in an angle of 180° (Fig. 11). This causes rephasing of the net magnetization since the slower spins that were ‘’lagging behind’’ are suddenly in front of the faster rotating spins. The net magnetization at the moment of complete spin refocusing is the one that produces the measured signal known as spin echo pulse[40,46]. The magnitude of the refocused magnetization is in principle different for each tissue. This is because different tissues in the human body have different relaxation constants. This allows the generation of contrast in T_2 or T_2^* - weighted images.

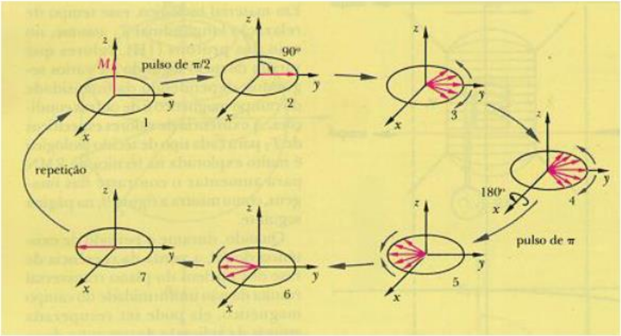

Figure 11: Schematic illustration of a spin echo sequence[46]

2.6.2. Gradient echo sequence

In a single gradient echo sequence a magnetic field gradient is applied in the direction of the main magnetic field. Due to this gradient, the field strength in the one side of a voxel will be lower than in the other side. Therefore, the spins along the voxel will precess with different frequencies, which will cause further dephasing. This dephasing effect is added upon the T_2 and T_2^* dephasing effects, so there will be a rapid decay in the signal. When the filed gradient is reversed a gradient echo appears[40,43]. This sequence compensates for the initial field gradient, not for T_2 or T_2^* effects.

2.7. Contrast agents in MRI

Different tissues in the human body have different T_1 or T_2 relaxation constants, a fact that yields contrast in the generated images. However, in most tissues the difference in T_1 or T_2 is not adequate to provide contrast and therefore reveal anatomical information. For this reason, contrast agents (CAs) are used for contrast enhancement[16,17,21,40,47–49]. Their importance is stated by the fact that up to 35% of the MRI sessions worldwide make use of CAs[48].

2.7.1. Quantification of the contrast enhancement

Contrast enhancement is measured by the relaxation rate:

$$R_i = \frac{1}{T_i}\ (s^{-1}), \qquad \text{for i} = 1{,}2 \qquad (9)$$

, where T_1, T_2 are the relaxation constants[16,21,47].

To evaluate the efficiency of a contrast agent, the relaxivity term is used:

$$r_i = \frac{R_i}{C}\ (mM^{-1}s^{-1}), \qquad \text{for i} = 1{,}2 \qquad (10)$$

, where R_i the relaxation rate and C the concertation of the contrast agent used[16,21,47]

In order to determine whether a material is T_1 or T_2 CA, the r_2/r_1 ratio is used. When $r_2/r_1 > 10$ the material is a T_2 CA, otherwise it is T_1 CA[16,21].

CAs affect tissues by shortening the relaxation time or by increasing the relaxation rate of protons around them, providing better contrast for anatomical regions:

$$R_{i,f} = R_{i,intr} + r_{i,ca} \leftrightarrow \frac{1}{T_{i,f}} = \frac{1}{T_{i,intr}} + r_{i,ca}C, \qquad \text{for i} = 1{,}2 \qquad (11)$$

, where $R_{i,f}$ $[s^{-1}]$ is the relaxation rate after adding the CA, $R_{i,intr}$ $[s^{-1}]$ is the intrinsic relaxation rate, $r_{i,ca}$ $[mM^{-1}s^{-1}]$ is the relaxivity of the CA, C [$\mathrm{mmol}^{-1}\ \mathrm{l}^{-1}$] is the CA concentration and T_i $[s]$ is the relaxation constant[16,21,47].

There are two types of CAs used in MRI: (a) paramagnetic contrast agents, which shorten T_1 relaxation times and (b) superparamagnetic contrast agents, which shorten T_2 relaxation[16,17,21,40,47–49].

2.7.2. T1 contrast agents

T_1 contrast agents reduce the T_1 relaxation time of surrounding protons, leading to brighter contrast in T_1 weighted images. T_1 CAs are based on paramagnetic metal – ions presenting net magnetization because of unpaired electrons. The most commonly used metal – ions are gadolinium (Gd^{3+}) or manganese (Mn^{2+}). However, gadolinium and manganese ions are toxic, so a chelating process is applied before their use as CAs, in order to avoid toxicity[16,17,21,48].

2.7.3. T2 contrast agents

T_2 contrast agents reduce the T_2 relaxation time of protons in the tissue of interest, thus lowering the signal intensity in a T_2 weighted image. The most commonly used T_2 CAs are SPIONs. When SPIONs are delivered into the tissue of interest during an MRI scan, their large magnetic moments induce magnetic field gradients making the total magnetic field locally inhomogeneous (Fig. 12a). Water protons diffuse through the inhomogeneous magnetic field induced by the SPIONs (Fig. 12b) a fact that causes dephasing of proton spins. This dephasing decreases the T_2 relaxation time of protons thus lowering the signal intensity in T_2 or T_2* - weighted images[16,17,21,40,47–49].

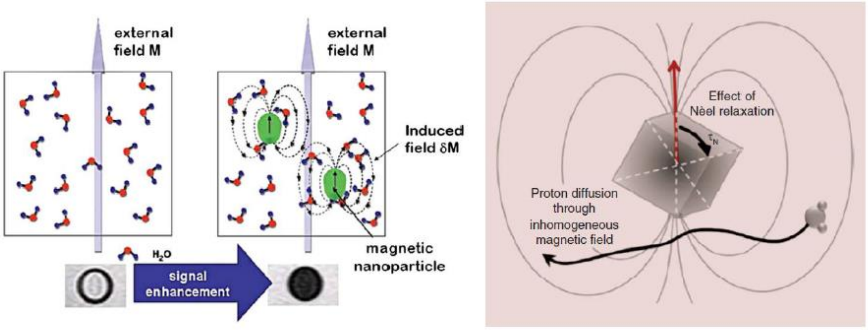

a) b)

Figure 12: a) Magnetic field gradients caused by SPIONs within a static magnetic field[48], b) diffusion of water protons through the inhomogeneous magnetic field created by the SPIONs[21]

2.8. SPIONs as T2 CAs

The relaxation rate induced to water protons by SPIONs is described by the outer sphere model:

$$R_2 = \frac{\alpha \gamma^2 N_A M \mu_c^2}{rD} \qquad (12)$$

, where α is a constant, γ is the gyromagnetic ratio of protons, M is the molarity of the nanoparticles, N_A is the Avogadro number, μ_c is the net magnetization of nanoparticles, D is the water diffusion coefficient and r is the effective radius of nanoparticles[21,50].

From equation (12) can be seen that the magnetic properties of SPIONs strongly influence the relaxation rate since $R_2 \propto \mu_c^2$. The magnetization in turn depends on size, shape and composition. Other properties affecting the relaxation rate are surface coating and aggregation state[16,17,21,47,51–54].

2.8.1. SPIONs saturation magnetization

The R_2 relaxation rate is proportional to the square of the magnetization. Therefore, the relaxivity increases for higher magnetization values. This behavior is observed because when the magnetization of SPIONs increases, the field gradients applied by the nanoparticles become stronger. Because of this, the dephasing of the water protons that diffuse through the SPIONs' environment is more pronounced, causing the shortening of protons' T_2 times and therefore the increase of r_2 relaxivities. This was experimentally demonstrated by Yoon et al.[55], whose research showed that as the magnetization of SPIONs increased, the relaxivity increased as well. This was tested for SPIONs with different chemical compositions, as can be seen in Fig. 13a.

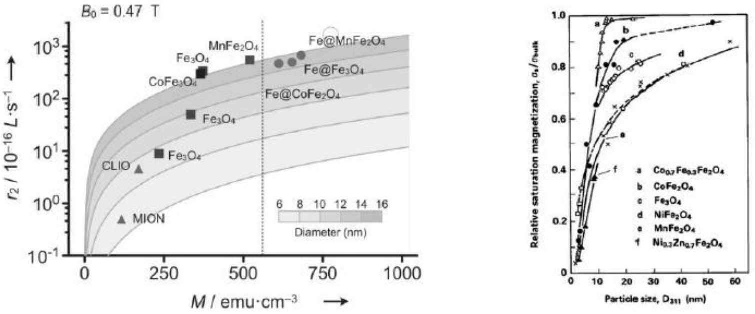

(a) (b)

Figure 13: (a) r_2 relaxivity values of particles with various chemical compositions as function of the particles' magnetizations and sizes[55], (b) Saturation magnetization values of different iron oxide nanoparticles as function of their sizes[48].

2.8.2. SPIONs size

Particle size is an important parameter for contrast enhancement. Increasing particle size results in an increase in magnetization values[47,51,54,56–59]. This behavior is attributed to the fact that net magnetization is proportional to the volume of SPION and volume increases with size[21]. At larger volumes spin canting is less significant and thus magnetization is higher in comparison with smaller sizes. Shokrollahi[48] showed that SPIONs larger in size correlate with greater saturation magnetization values (Fig. 13b).

Larger particles result in larger magnetization therefore, an increase in size should yield an increase in r_2 relaxivity[16,47,51,54–56,58,60]. This was demonstrated by Yoon et al.[55] according to Fig. 13(a) for SPIONs with different compositions. It is important to note that SPION size should not cross the critical size of the superparamagnetic regime (25nm for magnetite) since then ferromagnetic behavior emerges which gives rise to agglomerative behavior.

2.8.3. SPIONs composition

The composition of SPIONs is another property that can be tuned in order to increase the particles' saturation magnetization[16,21,35,47,61–64]. In principle a Fe atom can be replaced with a metal atom that exhibits a high magnetic moment, e.g. manganese (5 unpaired electrons) or cobalt (7 unpaired electrons), for example $Fe_3O_4 \rightarrow MnFe_2O_4$. This results in enhanced SPION magnetocrystalline anisotropy and increased saturation magnetization and thus high r_2 relaxivity. Yoon et al.[55] tested SPIONs with different compositions and demonstrated that $MnFe_2O_4$ particles resulted in higher relaxivities among several undoped and doped ferrite SPIONs, as can be seen in Fig. 13a.

2.8.4. SPIONs shape

An increase in anisotropy leads to larger net magnetizations in SPIONs. Anisotropy can be tuned via various ways. One way is doping SPIONs with other metal atoms, where the magnetocrystalline anisotropy is altered, leading to relaxivity enhancement. Yet another way is by changing the morphology of the SPION, where the shape anisotropy is altered, influencing the net magnetization and thus r_2 relaxivity[21,52,60,65]. In general it is known that cubic SPIONs present higher shape anisotropy than spherical SPIONs[50]. Moreover, cubic SPIONs present lower surface anisotropy when compared to spherical SPIONs. This is because spheres have more curved surface and therefore spin canting is more pronounced. Spin canting leads to lower magnetization and thus lower transverse relaxivity. In general spherical SPIONs have relatively low r_2 relaxivity[50] whereas cubic SPIONs have extremely high relaxivities as demonstrated by Lee et al.[66] for cubic 22 nm SPIONs, $r_2 = 761\ mM^{-1}s^{-1}$ at 3 T.

2.8.5. SPIONs coating

Coating of the surface of SPIONs with organic molecules in order to increase colloidal and biological stability can affect r_2 relaxivity. Relaxivity is related to the diffusion of water molecules around the SPION's environment. The nature of coating can either: (a) exclude water protons from diffusing near the SPIONs or (b) increase their residence time near the magnetic core of SPIONs. In the first case, the coating is of hydrophobic nature and leads to reduced relaxivity[67]. In the second case, hydrophilic coatings allow the circulation of water proton near SPIONs and thus increase r_2 relaxivity[63]. Polymer coatings belong to the hydrophilic category, with dextran and Polyethylene glycol (PEG) being the most commonly used polymers[16,21,49]. Duan et al.[67] studied the contribution of hydrophilicity to contrast enhancement by measuring the relaxivities of 10 nm SPIONs coated with polymers of increased hydrophilicity (Fig. 14). The results showed that the polymer with the highest hydrophilicity (hyperbranched polyethylenimine - PEI) lead to the highest r_2 relaxivity.

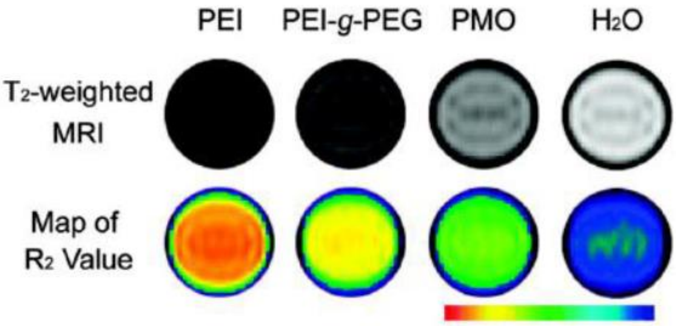

Figure 14: T_2-weighted images and R_2 color maps of 10 nm SPIONs with increasing (to the left) hydrophilicity[67]

Coating thickness also contributes to the r_2 relaxivity. Several studies have shown that when the thickness increases, a drop in the r_2 value is observed[68–70]. Tong et al.[68] synthesized SPIONs of 14 nm core size coated with the polymer PEG. MRI studies at 7 T showed than an increase in coating thickness from 1.97 nm to 8.43 nm resulted in a 2.5 – fold decrease in r_2 relaxivity. Increased coating thickness might interact with the surface atoms of the particles and form a magnetically dead layer and thus cause significant spin canting, which reduces the magnetization. Transverse relaxivity depends on the magnetization, therefore a decrease of the latter results in lower relaxivity.

2.8.6. SPIONs aggregation state

The aggregation state of SPIONs greatly affects the contrast enhancement performance. Studies have shown that multi core clusters comprised of smaller single core nanoparticles, yield a significantly higher magnetic moment and relaxivity than single core particles[47,71,72].

Chen et al.[71] developed monodisperse single core SPIONs and multi core SPION clusters (consisting of 8 single core particles on average), coated with the same copolymer (Fig. 15a), of hydrodynamic size 23 *nm* and 58 *nm*, respectively (Fig. 15b). Measurements of saturation magnetization resulted in higher magnetization for the multi core clusters in comparison to the single core SPIONs, while both showed superparamagnetic behavior (Fig. 16b). Transverse relaxation studies demonstrated an increase in the R_2 relaxation rate for the multi-core particles compared to the single core particles for varying iron concertation, as can be seen in Fig. 16a. This significant enhancement in MRI contrast effect may be attributed to the synergistic magnetism of multiple SPIONs[17,21].

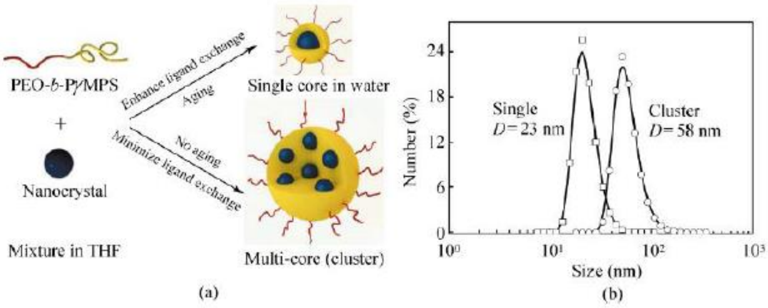

Figure 15: a) Schematic representation of multi-core and single core SPIONs, b) hydrodynamic size of cluster and single core SPIONs[71]

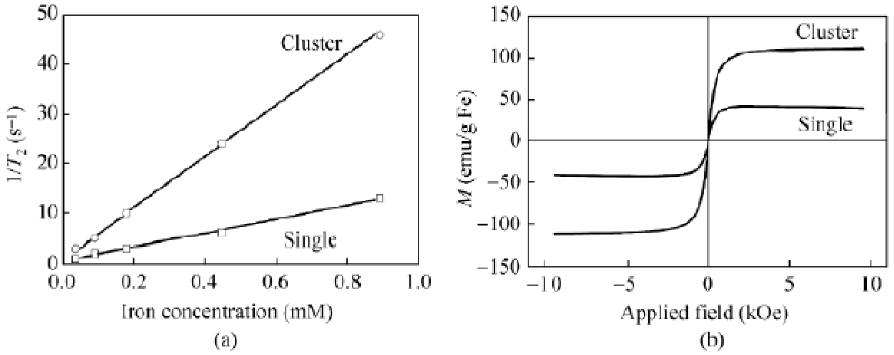

Figure 16: a) Transverse relaxation rate values for multi-core and single core SPIONs for varying concentration, b) magnetization curves for multi-core and single core SPIONs[71]

3 Materials and Methods

3.1. Pd – SPIONs synthesis and functionalization

Iron oxide nanoparticles with Pd core were synthesized using the protocol described by Liu et al.[73]. Different samples with varying sizes and shapes were obtained, namely E47, E55, E56, E63, E68 and E69. During synthesis all samples were coated with by a combination of oleic acid/oleylamine as a result of the thermal decomposition synthesis method via which they were made. These samples were provided by the ARI group of the RID. All samples were dissolved in hexane and were structurally and magnetically characterized and their performance as heating agents was investigated.

The Pd – SPIONs that presented high heating rates were also tested as T_2 contrast agents. The surface of these samples was modified and particles were next coated with hydrophilic surfactants to make them soluble in water and prevent particle aggregation. Dimercaptosuccinic acid (DMSA) and DSPE – PEG_{2000} COOH surfactants were used for the coatings. These samples were again provided by the ARI group of the RID and they were structurally and magnetically characterized and their contrast enhancing performance was measured.

3.2. Structural and Magnetic Characterization of Oleic Acid/Oleylamine coated Pd – SPIONs

A Jeol JEM-1400 plus Transition Electron Microscope (TEM) operating at an accelerating voltage of 120 kV was used to determine nanoparticle core size and shape. All samples for TEM were prepared by drop-casting the nanoparticle suspension in hexane on a Quantifoil R1.2/1.3 Cu 400. The solvent was evaporated at room temperature and the TEM images were obtained on the microscope. An electron beam of 120 keV was directed towards the target. At the target, part of the electron beam was scattered and the other part was transmitted through the sample, forming images of the nanoparticles on a fluorescent screen.

For the analysis of the TEM images the ImageJ software was used. In more detail, for each particle depicted, a 1D ROI was drawn as can be seen in Fig. 17 (yellow lines) and its length was measured. Taking into account the the scalebar present at the bottom left of each TEM image, the length of each particle was converted to nm. This was done for all particles in multiple images of each sample. The average and stadard deviation of all particle lengths was calculated in order to determine the particles' core size of each sample.

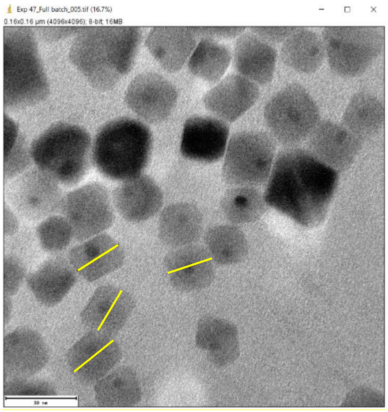

Figure 17: ROI selection in each particle for the size calculation with ImageJ.

The hydrodynamic size and aggregation state of nanoparticles were assessed by Dynamic Light Scattering (DLS) measurements using a Zetasizer Nano ZS setup. For those experiments a 4 mW, 633 nm He-Ne laser beam was directed towards nanoparticles in hexane solution. Light scattering measurements were performed over time at 173.5° scattering angle and the scattered light was detected by a photon detector. For each sample a concentration of 1 mg/ml was sonicated before the measurements in order to reduce aggregation. This step was performed to ensure that more small particles would be in solution and could be thus measured. To perform the measurements each sample was transferred into a PMMA cuvette viable for DLS measurements.

A Quantum Design MPMS-5S SQUID Magnetometer (5 T magnet) was used for the magnetic characterization of the nanoparticles. For those experiments each sample in powder form was moved up and down in an external magnetic field and produced an alternating magnetic flux which was picked up by a coil connected to the SQUID detector. The magnetic flux was converted to voltage which was then amplified to indicate the magnetism of the sample. The weight of each sample used for the measurements is shown in Table 2. Hysteresis loops at 5 K, 50 kOe and 310 K, 500 Oe were obtained. Properties like saturation magnetization, remanent magnetization and coercivity for each sample were determined, using the PYTHON script written in Appendix I. Zero – field – cooled and field – cooled (ZFC – FC) curves were also constructed form the data. A PYTHON script was created in order to calculate the blocking temperature T_B from the maximum of the ZFC curve (see Appendix I).

3.3. Structural and Magnetic Characterization of DMSA and DSPE – PEG_{2000} COOH coated Pd – SPIONs

The Jeol JEM-1400 plus TEM setup was again used to give information regarding the core size and shape of the samples dispersed in water. The samples were prepared following the same protocol as described before for the case of the particles coated with oleic acid/oleylamine.

The hydrodynamic size and aggregation state of nanoparticles were again assessed by Dynamic Light Scattering (DLS) measurements using a Zetasizer Nano ZS setup. This time the laser beam was directed towards nanoparticles in water solution and light scattering were performed over time at 173.5°. For each sample, a concentration of 1.5 mg/ ml was filtered in order to filter out any large aggregates and then measured. A filter of 25 mm diameter consisting of 0.22μm in size pores was used. Sonication was performed before the measurements in order to ensure that more small particles would be in solution and could be thus measured. To perform the measurements each sample was transferred into a PMMA cuvette viable for DLS measurements.

The Quantum Design MPMS-5S SQUID Magnetometer (5 T magnet) was used for the magnetic characterization of the nanoparticles in powder form. Hysteresis loops at 5 K, 50 kOe and 298 K, 50 kOe were obtained. In order to determine properties like saturation magnetization, remnant magnetization and coercivity for each sample, a PYTHON script was written and implemented (see Appendix I). The weight of each sample that was used for the measurements is shown in Table 5.

3.4. Calometric measurements

The magneTherm^{TM} digital device was used for the heating experiments of Pd - SPIONs. The working principle of the magneTherm^{TM} device was based on the inductor – capacitor (LC) circuit theory. The device consisted of LC circuits composed by a coil and sets of capacitors. Different combinations of capacitors were used to offer 10 different frequencies in the range from 50 kHz – 730 kHz. The tuning of each resonant frequency was done manually by the device everytime a set of capacitors was changed. For each given frequency there was an upper limit value for the magnitude of the magnetic field, with the device's upper limit being 25 mT. A sample was positioned within the coil of the device and an alternating magnetic field was produced, inducing heat via Néel or Brownian relaxation.

The coil inside the magneTherm device was hollow so that a constant rate of water could flow in it. This flow cooled the water from a chiller device set at 20 ^{o}C. This prevented the MagneTherm^{TM} device from overheating and it was also a way for the sample to cool down relatively fast after an exposure to an alternating magnetic field.

3.4.1. Calometric measurements in hexane

From each sample (E47, E55, E56, E63, E68 and E69) 5 mg in powder form were taken and solubilized in 1 ml hexane. Before any measurement each sample was vortexed and sonicated to increase colloidal stability and reduce aggregation. Ideally, calometric measurements and evaluation of SLP values are undertaken under adiabatic conditions, but such setups are difficult to build[19,24]. Therefore, experiments are usually performed under non – adiabatic conditions, a fact that compromises the accuracy of the evaluation of the SLP values[19,24]. In an attempt to reduce as much as possible any heat exchange between the heating sample and its surroundings, the sample was positioned inside a cylindrical – shaped, thermal insulating material made of foam, before it was placed within MagneTherm^{TM}'s coil.

During the heating measurements, two sensors (optical fibers) were used for the temperature recording. The first one was located at the center (point A) and the other at the right and bottom (point B) of the liquid sample, respectively (Fig. 18). The sensor at point B was used as an indicator for precipitation. Whenever the temperature at point B was higher than the one at point A, it meant that the particles had sedimented.

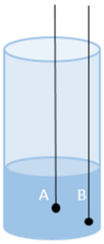

Figure 18: Schematic representation of the temperature recording within the sample. The temperature is measured at two points: (a) point A, at the center of the sample and (b) point B, at the bottom right of the sample

For each sample, standard measurements were performed (all available AMF frequencies and the maximum field strength of each frequency at each time). The time of exposure to the AMF field was set to 60 sec and the temperature was recorded over this period of time as well as 60 sec after exposure, respectively.

Taking into account the structural and magnetic characteristics of the different samples and their heating performance under AMF exposure, a comparison was made in order to determine which properties were related with enhanced heating performance among the samples.

3.4.2. Calometric measurements in water

The sample E68 was next coated with the hydrophilic DMSA and transferred to water in order to ensure colloidal stability and reduce aggregation. The sample's heating performance was once again measured with MagneTherm^{TM}. To further reduce aggregation 1 ml of 0.5% xanthan solution was added to the sample. Eventually, 1 ml of 2% agar solution was further added to stabilize the particles. Regarding the agar solution preparation, 0.2 mg of agar powder was dissolved in 10 ml distilled water. The solution was boiled until the agar completely dissolved. Once dissolved, the solution was left to cool down for 5 minutes. Then the agar solution was mixed with the sample. The whole mixture was vortexed and sonicated and immediately added to liquid nitrogen.

The heating performance of the DMSA – coated E68 sample was compared with commercial heating agent nanoparticles (Hypermag® provided by NanoTherics) in order to further determine what would be the optimum properties that the particles should have for enhanced heating performance. A sample of 5 mg/ml concentration in distilled water of the Hypermag particles coated with DMSA was prepared and measured for all the given frequencies and their corresponding maximum field strengths.

The minimum concentration of the commercial particles that would cause considerable heating (a temperature increase of at least 1 ^{o}C over 60 sec of exposure) was determined. The particles were diluted to concentrations 5, 4, 3, 2, 1 mg/ml and 0.5, 0.4, 0.3, 0.2, 0.1 mg/ml and their heating performance was measured with the MagneTherm^{TM}.

3.5. SLP calculation during calometric experiments

The SLP for each given frequency – magnitude pair was calculated using the initial slope method and the modified law of cooling. The results were compared. For the initial slope method, the temperature slope was calculated in the time range from 5 sec to 15 sec. This time range was chosen since at earlier moments the temperature increase was not sharp but rather smooth, probably due to some delay in the temperature increase during the very first seconds. For this calculation a PYTHON script was written (see Appendix I). The temperature increase during exposure as well as the maximum temperature reached were also calculated. Graphs depicting the behavior of temperature over time were obtained. For the modified law of cooling, the cooling curve of each of the samples was exponentially fitted in order to estimate the cooling constant k (a PYTHON script found in Appendix I was used for the fitting). Using equation (8) and the slope calculated by the initial slope method, the corrected temperature slope was calculated for each temperature recording. Based on the new slope values the adiabatic curve was reconstructed and linearly fitted. The slope of the fitted curve was used for the calculation of the SLP value.

3.6. Relaxivity measurements

For the relaxivity measurements the samples that presented the best heating performance were further investigated. As the nanoparticles from E68 coated with DMSA presented agglomeration and heavy sedimentation, it was concluded that the DMSA coating needed improving. Thus, in order to reduce the aggregation tendencies of the samples and improve their colloidal stability, the E63, E68 and E69 samples were coated with DSPE – PEG_{2000} COOH.

Before the NMR measurements all samples were sonicated in order to reduce aggregation. From each sample 150 μl were taken and filtered into a 5 mm NMR tube, in order to filter out any aggregates that would hinder the outcome of the experiments. A filter of 25 mm diameter consisting of pores of 0.22 μm was used. The E63 sample was diluted three times while E68 and E69 two times (each time the filter was washed with 150 μl of mQ water) in order to enable the quantification of the relaxivities. The longitudinal and transverse relaxivity of the samples were measured with a 400MHz Agilent NMR spectrometer operating at 9.4 T. Each sample was placed within the magnet and subjected in an external magnetic field. A 400 MHz radiofrequency pulse was applied, exciting the sample's protons.

An inversion recovery (IR) sequence was used for the T_1 relaxation study, while for the T_2 study a CPMG sequence was applied. During IR an 180^o RF pulse inverted the magnetization in the longitudinal axis, which then recovered to rest situation with T_1 relaxation time. A second RF pulse tipped the recovered magnetization to the transverse plane where a signal was measured (Fig.19a). During CPMG an RF excitation pulse was applied, followed by multiple 180^o refocusing pulses. Spin echoes were formed at the mid-points between refocusing pulses (Fig.19b), with decreasing intensity due to T_2 effects. An echo time of 0.5 ms was applied while the length of the spin echo train was varied.

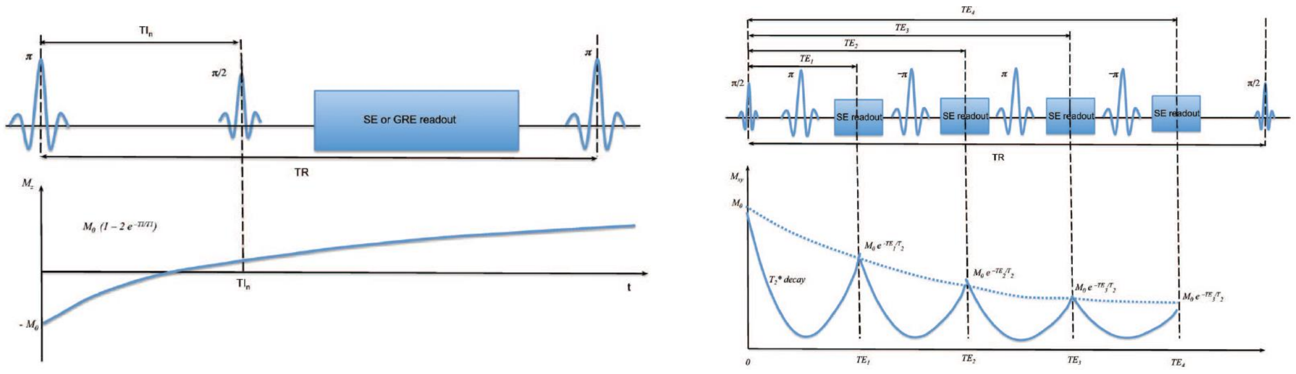

(a) (b)

Figure 19: A schematic of (a) inversion recovery sequence and (b) CPMG sequence

For the inversion recovery sequence 1 scan was taken, whereas for the CPMG sequence 4 scans were taken at 25 ^{o}C, respectively. During both sequences signal intensity was measured and plotted over time. The experimental points were fitted with the exponential function

$$Y = B + Fe^{-X*G} \tag{13}$$

where G corresponds to the $R_{1,\ 2}$ relaxation rate. All three samples were structurally and magnetically characterized and their performances as T_2 contrast agents were compared along with the commercial particles in order to estimate which properties were related with enhanced performance.

3.7. MRI and CT studies

MRI phantom and CT studies were performed using commercial nanoparticle samples with different concentrations. For the MRI studies, the commercial SPIONs provided by Hypermag were used. Three samples were prepared with concentrations of 4, 1, 0.4 mg/ml. The initial sample had a concentration of 10 mg/ml therefore it was diluted to obtain the three different samples of 1 ml volume each. Furthermore, each samples was mixed with 2% of agar solution of 1 ml volume in order to create phantoms which mimic breast tissue. From literature is known that 3 – 4% of agar gel mimics hard tissue, whereas lower content gels are similar to soft tissues as the human breast[74].

The agar solution was prepared as mentioned in section 3.4.2. Then 1 ml of each sample containing 4, 1, 0.4 mg/ml was mixed with 1 ml of 2% agar solution. Thus, the obtained concentrations were 2, 0.5, 0.2 mg/ml of particles in agar solution (0.01 mg/ml of agar). The samples were vortexed and sonicated and then cooled down in a refrigerator until the solution solidified. When the samples were ready, they were used for the MRI studies (Fig. 20a).

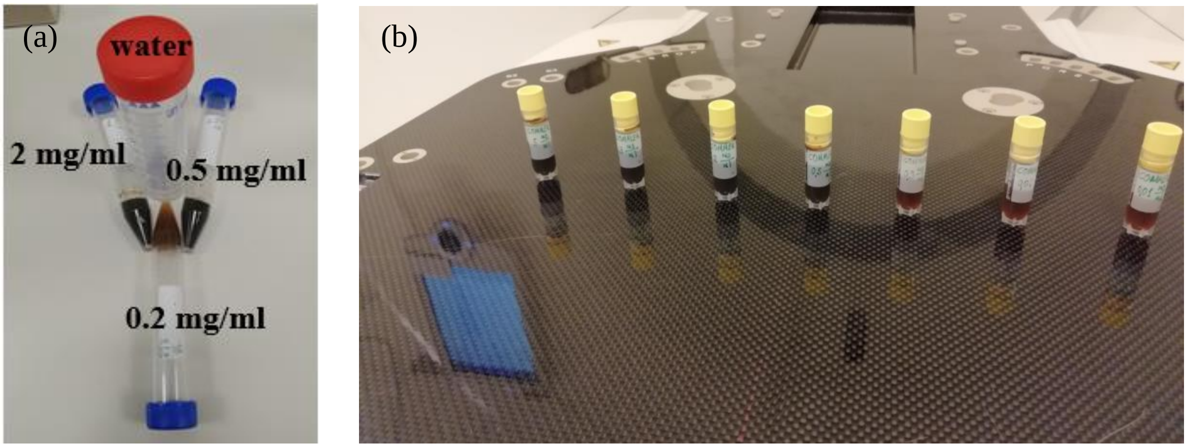

Figure 20: (a) Phantom containing commercial particles used in MRI studies, (b) Commercial particles of different concentrations used in CT studies, from left to right: samples with concentrations of 5, 3, 2, 0.5, 0.3, 0.2 and 0.1 mg/ml

For the MRI studies a GE Medical Systems scanner operating at 1.5 T was used. An R_2* IDEAL IQ Multi Echo Gradient Echo sequence and a Zero Echo Time Sequence were used. The Multi Echo Gradient Echo sequence can be seen in Fig 21a. After the excitation pulse, a series of alternating gradients was applied. Each time a gradient was reversed an echo was measured. Due to T_2* effects the intensity of the signal at each following echo time was decreased. The IDEAL IQ had the following parameters: TR = 12.57, TE = 3.91, number of echoes 1, echo train length 6, matrix size 96 x 96, pixel bandwidth 651 Hz, flip angle 7, slice thickness 2 mm, spacing between slices 2 mm.

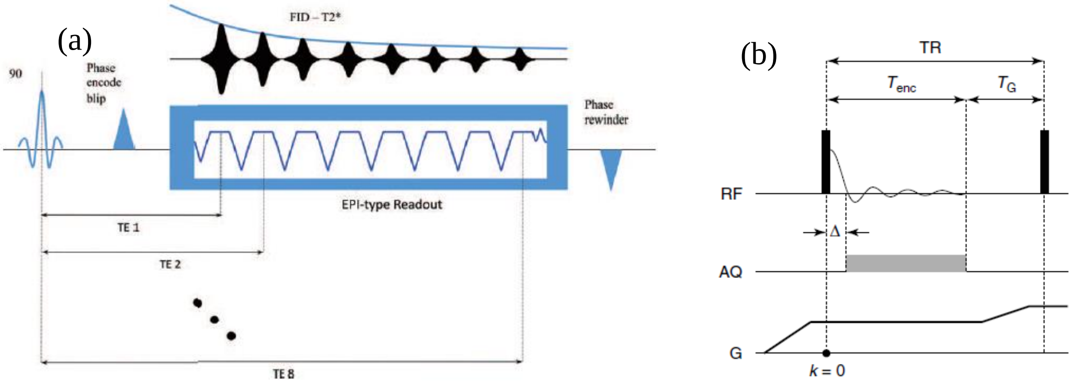

Figure 21: A schematic of (a) Multi Echo Gradient Echo sequence and (b) Zero Echo Time sequence

The Zero Echo Time Sequence can be seen in Fig. 21b. A gradient of amplitude G was first ramped up and then the RF excitation pulse was applied. Therefore, gradient encoding was performed immediately at a very fast speed, hence resulting in an actual zero echo time. The Zero Echo Time Sequence had the following parameters: TR = 509.22, TE = 0.02, number of echoes 1, echo train length 1, FOV 40 cm, matrix size 160 x 160, pixel bandwidth 488 Hz, flip angle 3, slice thickness 2 mm, spacing between slices 2 mm.

For the CT study the commercial SPIONs provided by Hypermag were again used. Seven samples were prepared with concentrations of 5, 3, 2, 0.5, 0.3, 0.2 and 0.1 mg/ml (Fig. 20b). The initial sample had a concentration of 10 mg/ml therefore it was diluted to obtain the seven different samples of 1 ml volume each. A Siemens CT scanner with a tube setting of 120 kV was used. The acquisition parameters were: pitch 1.2, Table speed 46 mm/rotation, collimator width 19.2 mm

The ImageJ software was used for the analysis of the CT data and the determination of the HU of each sample at different concentrations. In more detail, for each sample, a 2D ROI was drawn as can be seen in Fig. 21 and the pixel values within this ROI where converted to HU. Two different CT images were used for the determination of HU of each of the seven samples. The mean and standard deviation of HU for each concentration were calculated.

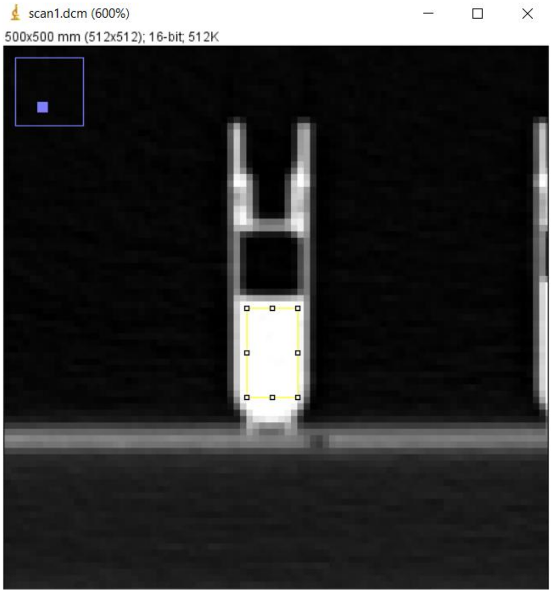

Figure 21: ROI selection with ImageJ for HU calculation of each commercial sample of different concentration

4 Results and Discussion

4.1. Structural Characterization for the Pd - SPIONs solubilized in hexane

The shape and core size (Pd core plus middle shell SPIO) of the six different Pd – SPION samples coated with oleic acid/oleylamine were assessed by Transmission Electron Microscopy (TEM) images shown in Fig. 22. The dark stains correspond to the Pd core while the surrounding grey shell corresponds to the iron oxide middle shell. The particles were all coated with oleic acid/oleylamine, however in TEM the surfactant is not detectable and thus only the size of the Pd – core and middle shell iron oxide could be measured.

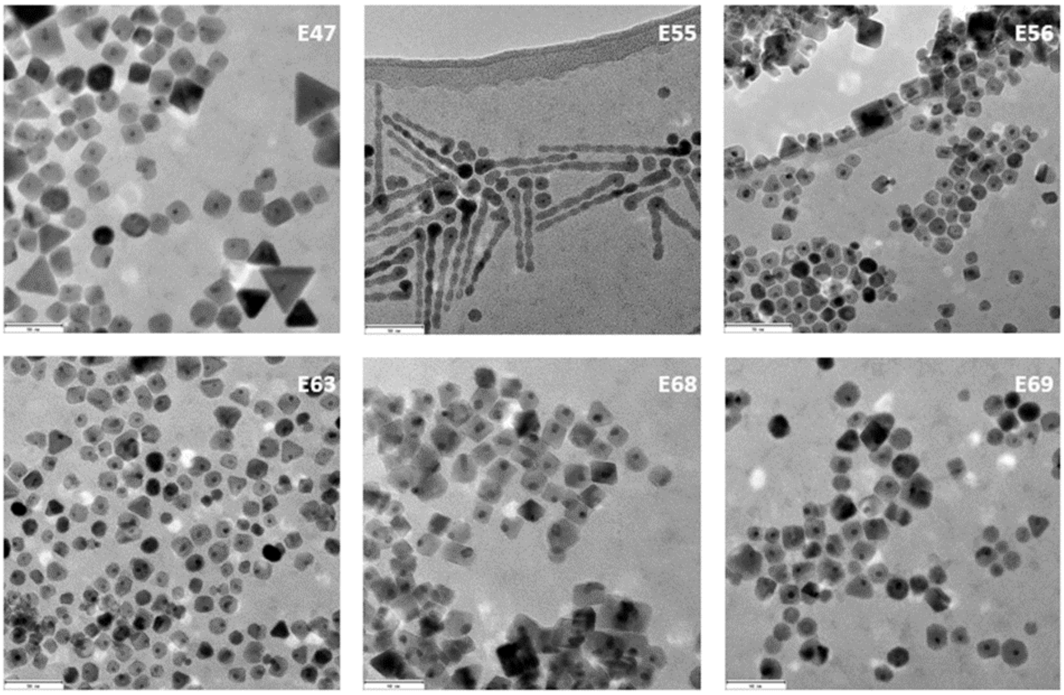

Fig. 22: TEM images of six different samples of Pd – SPIONs coated with oleic acid/oleylamine synthesized at the RID. Pd appears as dark dots while iron oxide as the grey shell surounding the Pd core.

The core sizes and shapes of the different samples are summarized in Table 1. Regarding the core sizes it can be seen that all nanoparticle samples, except E55, lied below the superparamagnetic regime – 25 nm diameter for iron oxides. However, in samples E47 and E56 bigger sizes than the ones reported in Table 1 could be also found (up to 50 nm) as can be seen in Fig. 22, a fact that increased the polydispersity of those samples. Regarding the sample E55 it is shown in Fig. 22 that it was made of worm – like particles, which consisted of a round shaped head and a long tail. For this reason two sizes are reported in Table 1, one corresponding to the round head followed by the the size of the tail.

By looking at the TEM images can be observed that in each sample the nanoparticles exhibited not only one single shape but more (cubes, spheres and triangles were present). However, in Table 1 the shape that the majority of the particles had is presented for each sample, since it was considered that this shape dictated the heating and contrast enhancing performance throughout this research.

Table 1: TEM and DLS data of the Pd – SPIONs coated with oleic acid/oleylamine and dispersed in hexane

Sample	D_{TEM} (nm)	Shape	D_{DLS} (nm)
E47	19 (2.55)	Cubic	156
E55	13.48 (2.37) and 80.12 (13.26)	Worms	98
E56	17.91 (2.13)	Spherical	459
E63	16.69 (2.27)	Spherical	1007
E68	15.47 (2.07)	Cubic	46
E69	15.34 (2.72)	Spherical	37

The hydrodynamic size (Pd core plus middle shell SPIO plus surfactant) of the tested nanoparticles was assessed by Dynamic Light Scattering (DLS) measurements. The results are shown in Fig. 23 (a) – (f), where the normalized intensity of the scattered laser beam was plotted as a function of nanoparticle size. The intensity peaks correspond to the amount of light that was scattered by particles with the corresponding size. In other words, DLS measurements gave an estimation of the hydrodynamic sizes of the particles present in the sample.

The DLS results in Fig. 23 (a) – (f) showed at least two intensity peaks for each sample, except for E55. In Table 1 the hydrodynamic size corresponding to the maximum intensity peak of the scattered light is presented for each sample, since it was considered that this size was of importance throughout this research. It can be seen that the DLS diameters were larger than the one obtained by TEM. The larger DLS sizes probably occurred due to the presence of the oleic acid/oleylamine coating or due to aggregation of nanoparticles which led to the formation of larger in diameter clusters. Intensity peaks corresponding to even larger sizes were also present within each sample due to further agglomeration of the particles.

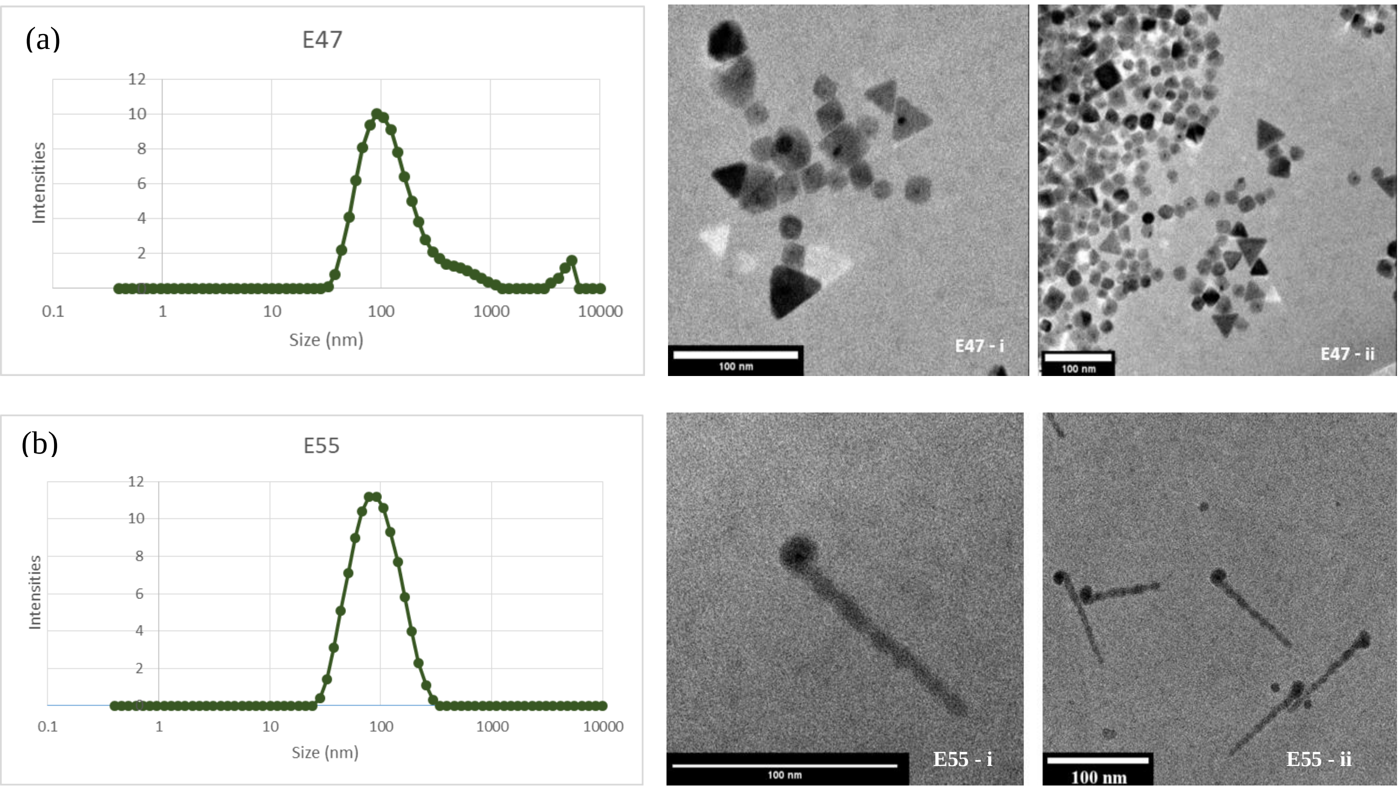

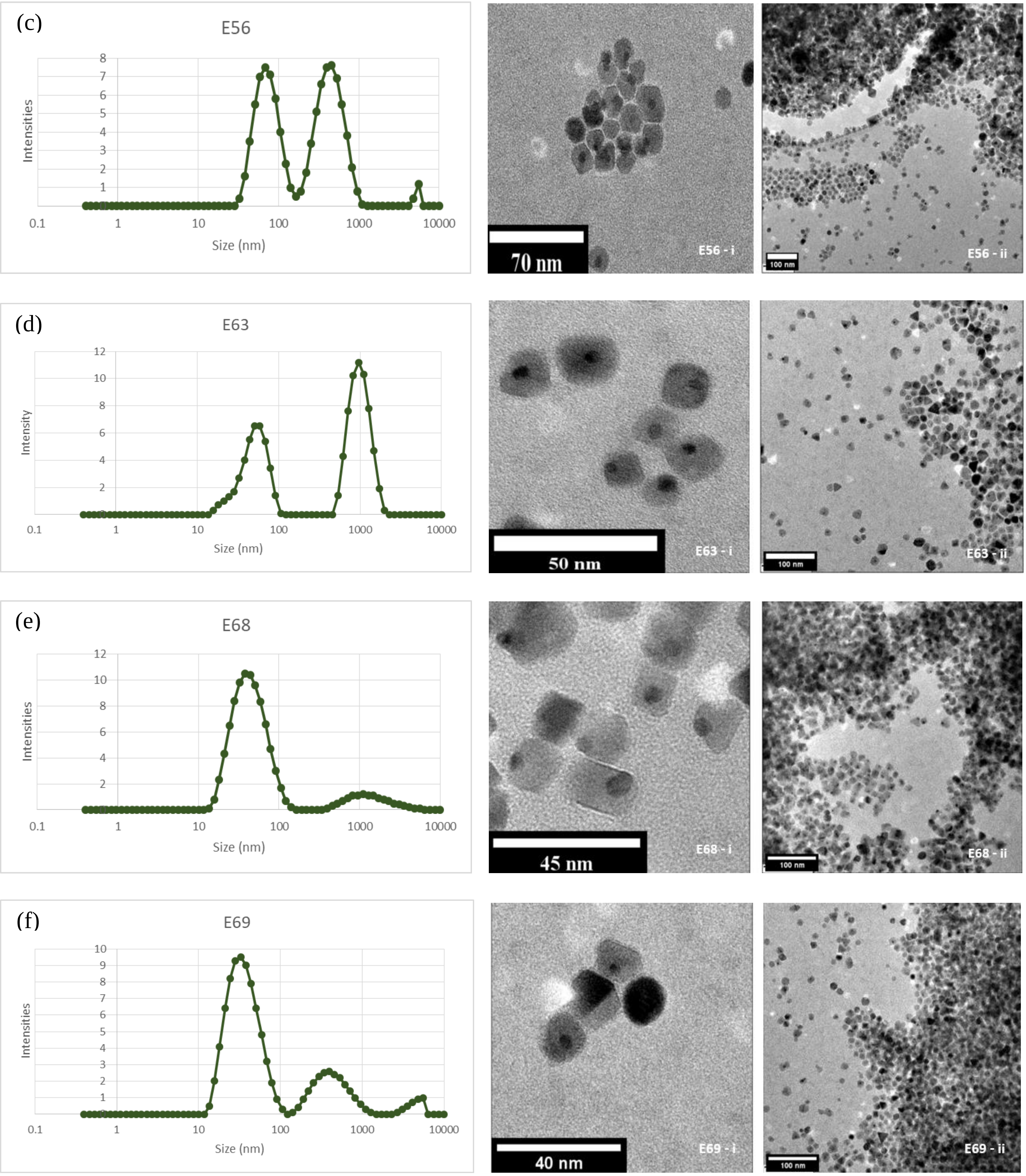

Fig. 23: DLS and TEM data of all Pd – SPION samples coated with oleic acid/oleylamine: (a) – (f) normalized intensity of the scattered laser beam as a function of hydrodynamic size

4.2. Magnetic Characterization for the Pd – SPIONs dispersed in hexane

Hysteresis loops at 5 K for all samples measured in powder form showed ferromagnetic behaviour with considerable coercivity and remanent magnetization, as can be seen in Fig. 24 and Table 2. From the previous results it was showed that all samples consisted of particles with sizes smaller that the size limit of the superparamagnetic regime. Therefore, it would be expected that the samples would neither show any remanent magnetization nor coercivity. To this regard the blocking temperature was calculated from the ZFC – FC graphs, as a further indication of whether the samples could lie in the superparamagnetic regime or not. Table 3 shows the blocking temperatures of all samples. It can be seen they are all higher than 5 K which was the temperature under which the experiment was conducted. Therefore, even though the sizes indicated that all samples were superparamagnetic, the thermal energy at a temperature of 5 K was not sufficient to randomly flip the magnetic moments of the particles and thus grant them the superparamagnetic status. For this reason, hysteresis loops at a higher temperature were taken. The weight of each sample measured is also shown in Table 2.

It should be noted at this point that for the application of MRI – guided thermotherapy the Pd - SPIONs will be intratumorally injected into a patient. Therefore, the magnetic behaviour of these samples at body temperature would be of interest. For this reason hysteresis loops at 310 K were measured. From Fig. 25 and Table 3 can be seen that both remanent magnetization and coercivity were zero, which indicated that the samples were in superparamagnetic state at 310 K. In addition, the magnetization for all samples at both temperatures was estimated and it is shown in Tables 2 and 3.

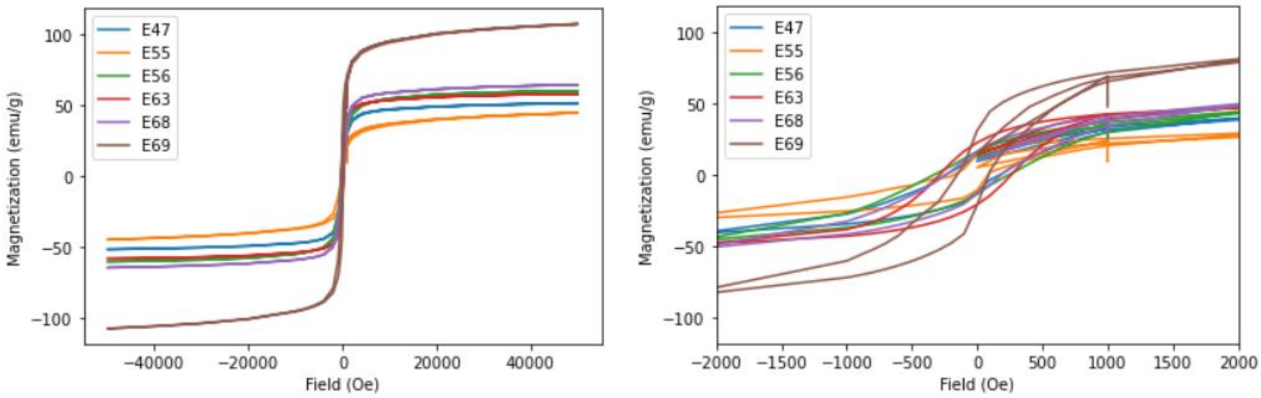

Figure 24: Left: Hysteresis loops of all Pd – SPION samples coated with oleic acid/oleylamine at 5K and 50 kOe. Right: Scale of x – axis was changed in order to show the remanent magnetization and coercivity values

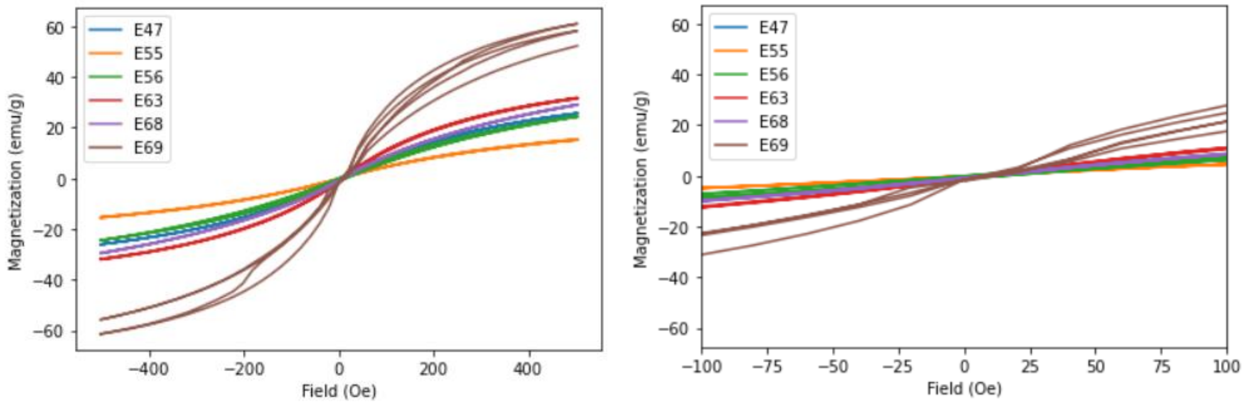

Figure 25: Left: Hysteresis loops of all Pd – SPION samples coated with oleic acid/oleylamine at 310 K and 500 Oe Right: Scale of x – axis changed in order to show the zero remanent magnetization and coercivity values

From Fig. 25a can be seen that samples did not reach saturation magnetization during those experiments since the applied field reached only a maximum value of 400 Oe (40 mT) which was not enough to saturate the magnetization of the samples. This however, was not a problem since with MagneTherm^{TM} the heating experiments were performed for an AMF with a magnitude of 19 mT, so the samples did not reach their saturation magnetization as well in those experiments. Thus, in order to determine which magnetic properties led to better/pooper heating performance, the magnetic characterization was performed under the same conditions as the heating experiments. In Table 3 the magnetization of each sample at 19 mT is presented.

Table 2: Remanent Magnetization and Coercivity of the different Pd – SPION samples at 5 K for 50 kOe. The weight of each sample and its saturation magnetization are also shown. Uncertainty in weight was 0.04 mg, whereas the error in measurement of magnetization was 0.01 emu, the propagated error was 0.01 emu/g for all measurements

Sample	Weight (mg)	M_r (emu/g)	H_c (Oe)	Ms (emu/g)
E47	1.21	14.55	250	51.75
E55	1.39	14.68	150	44.88
E56	1.21	16.56	350	60.39
E63	1.19	22.75	250	58.22
E68	1.46	16.03	250	60.53
E69	0.92	31.27	150	107.84

Table 3: Saturation magnetization of the different Pd – SPION samples at 310 K and 500 Oe. Remanent Magnetization and Coercivity were zero for all samples. Blocking temperature is also depicted. Uncertainty in magnetization was 0.01 emu/g

Sample	T_B (K)	M_s (emu/g)
E47	247	14.58
E55	119	8.49
E56	124	13.34
E63	102	19.27
E68	230	15.60
E69	132	39.66

From Table 1 and 3 can be seen that even though sample E68 consisted of cubic particles, its magnetization value was lower than E63's and E69's which were made of spherical particles. In general, cubic morphology leads to higher shape and thus effective anisotropy and less significant spin canting effect than spherical shape. Thus, it would be expected that the E68 would present higher magnetization in comparison with E63 and E69. Magnetization depends on the effective anisotropy, but contribution in anisotropy can be also made via the magnetocrystalline anisotropy. The reason for the higher magnetizations of samples E63 and E69 might possible lie in the fact that their crystal structure resulted in higher magnetocrystalline anisotropy compared to the E68 sample and thus higher magnetization values. Further experiments with Mossbauer spectroscopy could reveal information about the crystal structure of the samples.

4.3. Structural Characterization for the Pd - SPIONs in water

The TEM images of the samples E63, E68 and E69 coated with DSPE - PEG_{2000} COOH can be seen in Fig. 26, while in Fig. 27 the E68 and the commercial Hypermag particles coated with DMSA are illustrated. As previously discussed, the dark dots in Fig. 26 correspond to the Pd – core, whereas the grey middle shell surrounding Pd is the iron oxide. The commercial particles consist only of iron oxide. The core size and shape of the particles of each sample are summarized in Table 4. In contrast with the TEM images of Fig. 22, the Pd – SPION samples were coated with DSPE - PEG_{2000} COOH and DMSA and were dispersed in water. The core sizes and shapes of the samples were not expected to be any different from the ones reported in Table 1, thus all samples still fell in the superparamagnetic range regarding size.

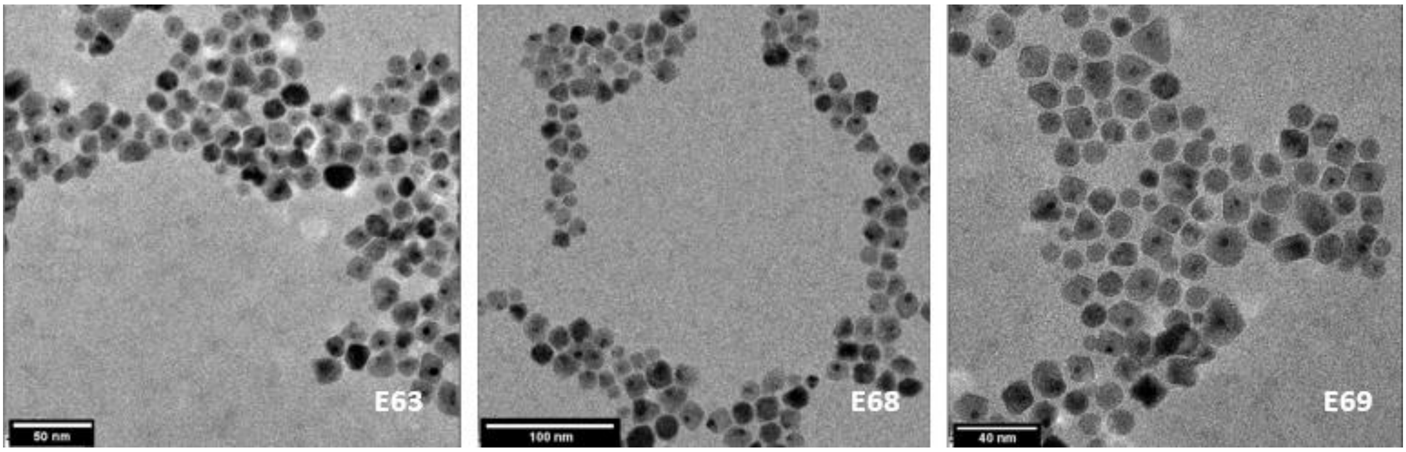

Figure 26: TEM images of Pd – SPIONs coated with DSPE - PEG_{2000} synthesized at the RID. Pd appears as dark dots while iron oxide as the grey shell surrounding the Pd core.

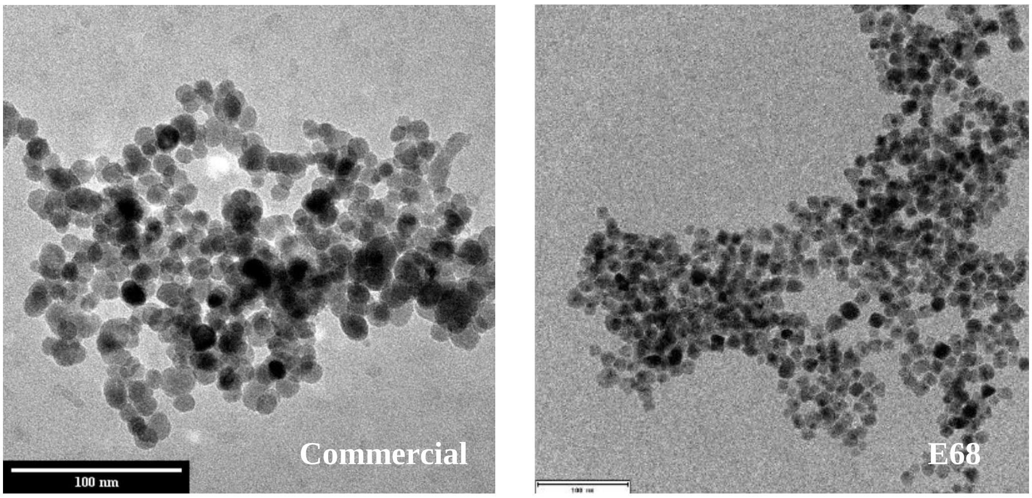

Figure 27: TEM images of Pd – SPIONs synthesized at the RID and commercial Hypermag particles coated with DMSA. Right: Pd appears as dark dots while iron oxide as the grey shell surrounding the Pd core, left: only iron oxide is present as grey dots

The hydrodynamic size of each sample coated with DSPE - PEG_{2000} COOH as well as with DMSA (only E68) was assessed with DLS measurements. The results are depicted in Fig.28, where the normalized intensity of the scattered laser light is plotted as a function of nanoparticle size. The hydrodynamic sizes of each sample are summarized in Table 4. It can be seen that the DLS diameter was larger than the one obtained by TEM. This could be attributed to the presence of surfactant or agglomeration of the nanoparticles which led to the formation of larger in diameter clusters.

Table 4: TEM and DLS data of the Pd – SPIONs coated with DSPE – PEG_{2000} COOH and E68 and commercial samples coated with DMSA dispersed in water. For commercial particles values were taken from the manufacturer's specifications

Sample	D_{TEM} (nm)	Shape	D_{DLS} – DSPE PEG_{2000} COOH (nm)	D_{DLS} – DMSA (nm)
E63	16.69 (2.27)	Spherical	110	-
E68	15.47 (2.07)	Cubic	88	154[75]
E69	15.34 (2.72)	Spherical	85	-
Commercial	15.2	Spherical	-	100

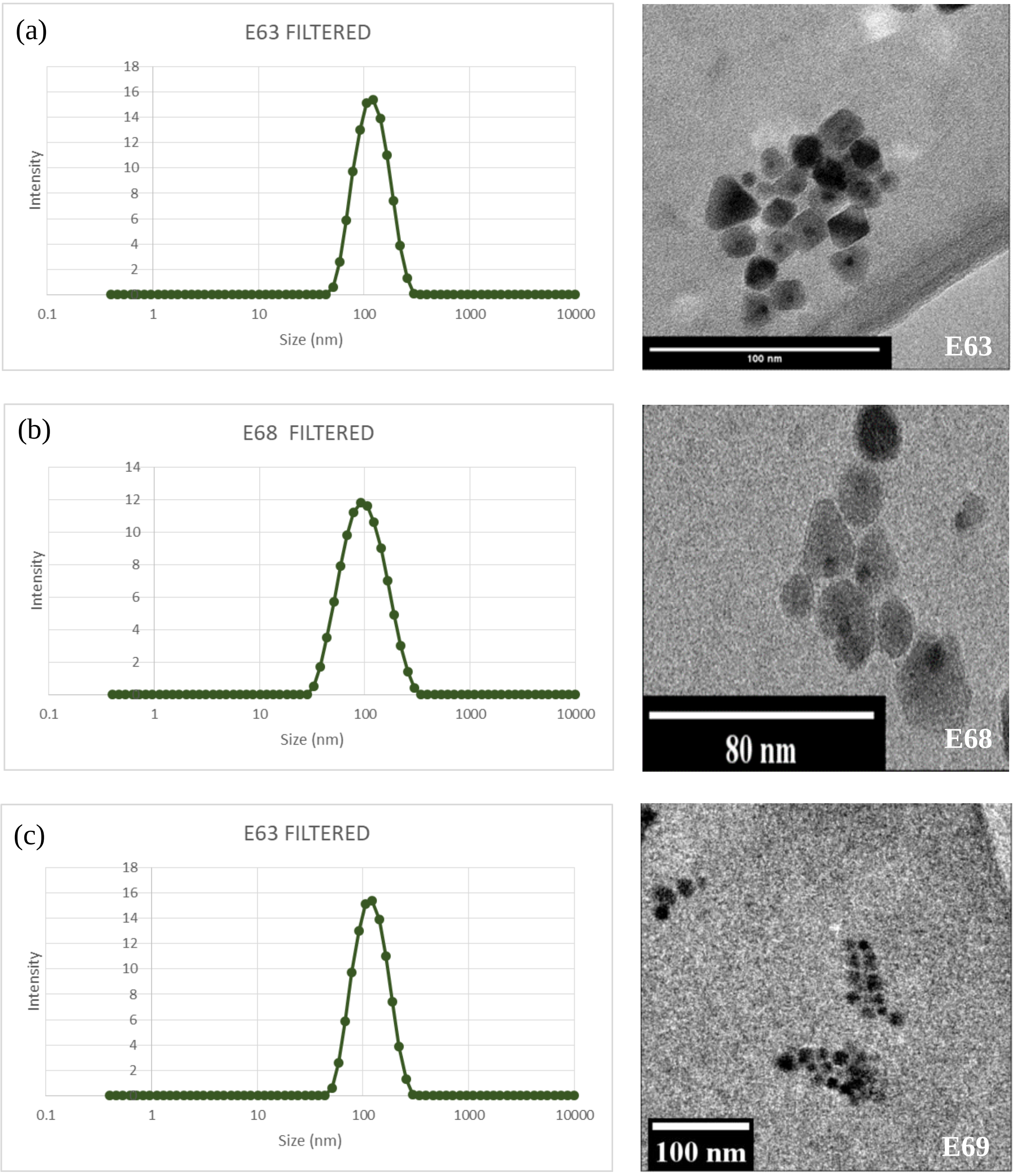

Figure 28: DLS and TEM data of all Pd – SPION samples coated with DSPE – PEG_{2000} COOH: (a) – (c) normalized intensity peaks of the scattered laser beam as a function of hydrodynamic size

4.4. Magnetic Characterization for the Pd - SPIONs coated with DSPE – PEG$_{2000}$ COOH and commercial particles coated with DMSA

Hysteresis loops were obtained for Pd - SPION samples coated with DSPE – PEG$_{2000}$ COOH at 5 K, 50 kOe. The samples showed ferromagnetic behaviour since they presented considerable remanent magnetization and coercivity as can be seen in Fig. 29. This was expected since at 5 K samples were below the blocking temperatures shown in Table 3. The weight of each measured sample as well as its saturation magnetization at 5 K are presented in Table 5. The hysteresis loop of the commercial particles coated with DMSA is also shown for comparison purposes in Fig. 29.

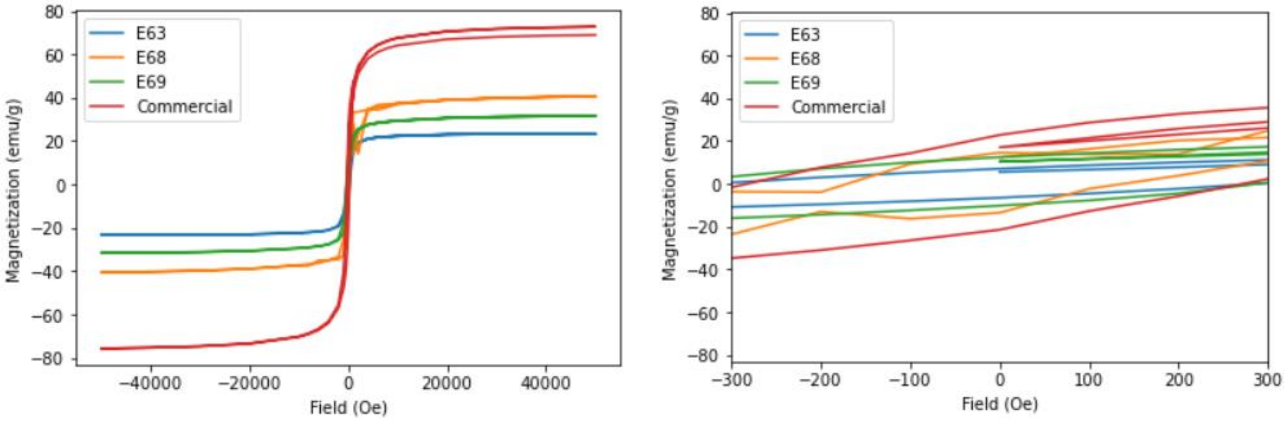

(a) (b)

Figure 29: Hysteresis loops of Pd - SPION samples coated with DSPE – PEG$_{2000}$ COOH and commercial particles coated with DMSA at (a) 5 K and 50 kOe, (b) Scale of x – axis changed in order to show the remanent magnetization and coercivity values

The functionalization of each synthesized sample with different surfactants (oleic acid/oleylamine and DSPE – PEG$_{2000}$ COOH) resulted in a decrease in saturation magnetization at 5 K, as can be seen in Fig. 30 and Table 6. This can be due to the fact that for the surfactant exchange step the oleic acid/oleylamine coated particles were encapsuled in DSPE – PEG$_{2000}$ COOH, which caused the increase of the coating thickness. This fact led to more pronounced spin canting effects and thus lower magnetization values.

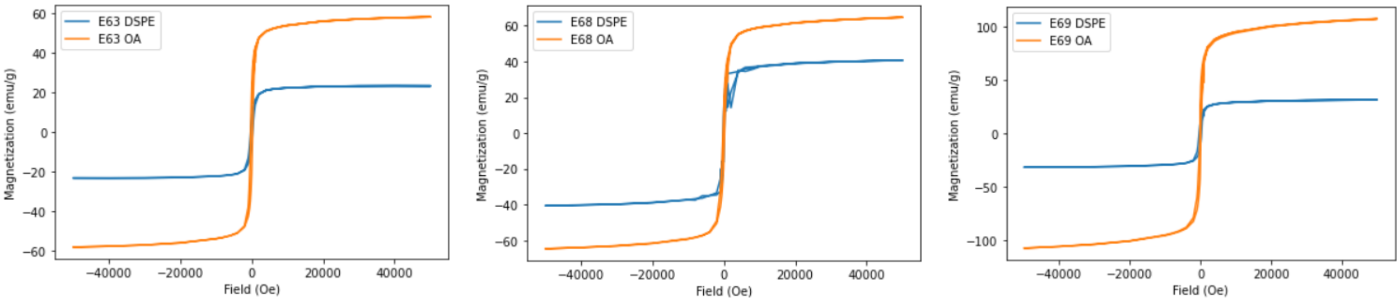

Figure 30: Hysteresis loops of each Pd - SPION sample with different coatings. Saturation magnetization decreased when the oleic acid/oleylamine surfactant was replaced with a DSPE – PEG$_{2000}$ COOH one.

Table 5: Saturation magnetizations of the different Pd – SPION samples at 5 K and 298 K for 50 kOe. The weights of each sample are also shown. Uncertainty in weight was 0.04 mg, whereas the error in measurement of magnetization was 0.01 emu, the propagated error is shown for all measurements

Sample	Weight (mg)	Ms (emu/g) at 5K	Ms (emu/g) at 298K
E63	0.520	23.33 (0.02)	19.51 (0.02)
E68	0.940	40.64 (0.01)	35.62 (0.01)
E69	0.460	31.62 (0.02)	26.64 (0.02)
Commercial	1.16	72.70 (0.01)	-

Table 6: Saturation magnetizations of Pd – SPION samples with different coatings at 5 K

Sample	Ms (emu/g) - OA	Ms (emu/g) – DSPE – PEG_{2000} COOH
E63	58.22 (0.01)	23.33 (0.02)
E68	60.53 (0.01)	40.64 (0.01)
E69	107.84 (0.01)	31.62 (0.02)

The magnetization of the samples was investigated at 298 K, 5 T. This temperature was higher than the blocking temperature of each sample, therefore the nanoparticles were superparamagnetic. In order to determine which magnetic properties led to better/pooper contrast enhancing performance, the magnetic characterization was performed under the same conditions as the NMR experiments. The NMR used a field of 9.4 T and was performed at 298 K temperature. However, during the magnetization measurements the maximum filed was limited to 5 T. As it can be seen at Fig. 31, the magnetizations of all three samples were already saturated at this field strength, thus it can be assumed that the value of saturation magnetization at 9.4 T would be the same as for 5 T. The saturation magnetizations of each sample at 298 K are summarized at Table 5.

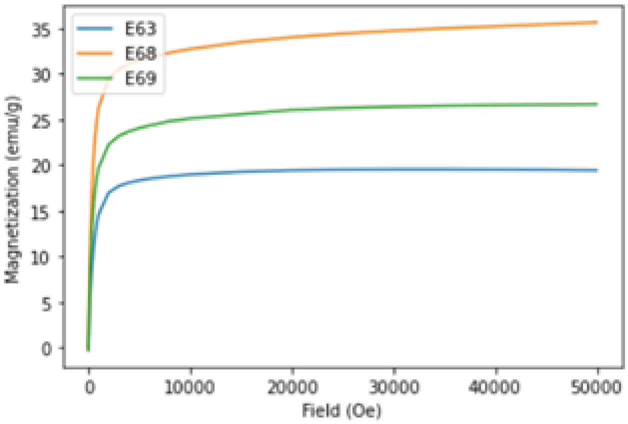

Figure 31: Hysteresis loops of Pd - SPION samples coated with DSPE – PEG_{2000} COOH at 298 K and 50 kOe (5 T)

4.5. Calometric measurements

The heating performance of all six different Pd - SPION samples dispersed in hexane was tested with MagneTherm^{TM}. The goal was to discover which particle parameters were related with better/poorer heating performance and conclude which would be the optimal properties of particles to be used as heating agents in thermotherapy.

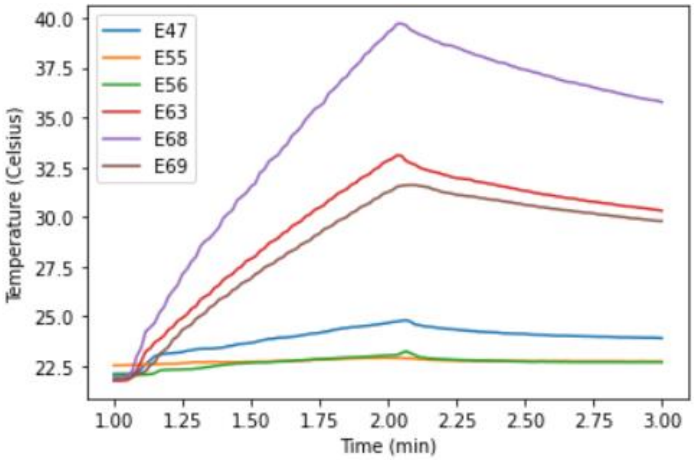

Figure 32: Temperature profile over time for six different Pd - SPION samples coated with oleic acid/oleylamine and dispered in hexane. The temperature was recorded for one minute during AMF exposure and one minute after exposure. An AMF of 345 kHz frequency and 19 mT magnitute was exerted on the particles

To demonstrate the different performances of all six samples, their temperatures during one minute of AMF exposure and one minute after exposure were recorded over time, as can be seen in Fig.32. All the samples were tested for multiple frequency – magnitude combinations. According to the LRT model, SLP values increase with increasing field frequency and magnitude (see section 2.5.7). According to Fig. 33 the SLP values of Pd – SPIONs (green dots) were in good agreement with the theory (orange dotted lines) for both amplitude and frequency dependence, indicating that the heating performance of these particles can be predicted by the LRT model. The frequency and magnitude values that resulted in the higher SLP values are discussed, 345 kHz and 19 mT, respectively since interest was placed on the conditions under which the highest heating rates were obtained for each sample. The other frequency – magnitude combinations tested with MagneTherm^{TM} during the standard measurements, were either lower in frequency or magnitude than the 345 kHz - 19 mT pair and thus resulted in lower SLP values.

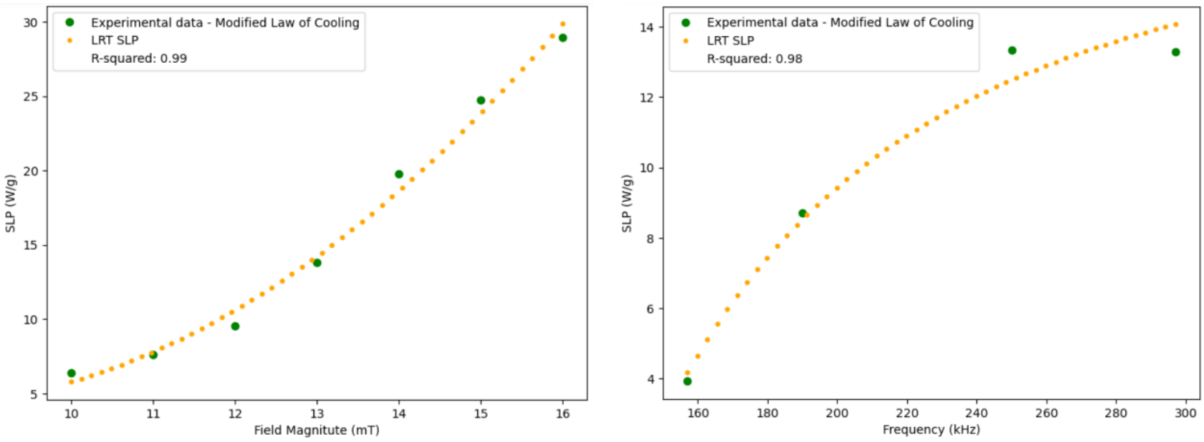

Fig. 33: SLP values plotted as a function of AMF magnitude (left) and frequency (right). The experimental values were in good agreement with the LRT model for both amplitude and frequency dependence.

The calculated SLP values using the initial slope method (ISM) and the modified law of cooling (MLC), the temperature increase during one minute of AMF exposure as well as the maximum temperature reached for each sample are presented in Table 7. The SLP value calculated using MLC was more accurate since external heat losses were taken into account for the calculation. From Table 7 can be seen that the maximum percentage difference between the SLP values calculated with the two different methods, was 11.53 % for sample E69. In literature, differences up to 21% have been reported[76]. The lower percentage difference obtained during the experiments with MagneTherm^{TM} can be due to the thermal insulating material that the samples were placed into during the measurements, which reduced heat losses towards the environment.

From Fig. 32 and Table 7 can be seen that out of the six samples, half present high heating rates (E63, E68 and E69) and the other half present low heating performance (E47, E55 and E56) – they will be called samples of Group A and samples of Group B, respectively. Looking at the results, E68 outperformed the rest of the samples given that in one minute of exposure the calculated SLP value was 91.86 W/g, the temperature increased 17.34 °C in one minute of AMF exposure and reached a maximum of 39.26 °C. The sample with the poorer performance was the E55 with a SLP of 1.67 W/g, an increase of only 0.38 °C was seen and up to 22.92 °C. In order to evaluate which particle properties were related with better/poorer heating performance, the influence of structural and magnetic motifs on the heating performance was investigated.

Table 7: Results of the heating experiments for six different Pd - SPION samples coated with oleic acid/oleylamine and dispered in hexane. The uncertainty in temperature measurement was 0.01 °C taken my multiple measurements under the same conditions, the propagated error in SLP was calculated for all measurements

Sample	T increase (°C)	Maximum T (°C)	SLP_{ISM} (W/g)	SLP_{MLC} (W/g) *	% SLP difference
E47	2.56	24.67	22.0 (1.7)	22.07	0.31
E55	0.38	22.92	1.6 (0.1)	1.67	5.54
E56	0.99	23.04	6.0 (0.4)	5.8	3.38
E63	11.04	32.82	51.2 (4.2)	51.22	0.04
E68	17.34	39.26	81.5 (6.5)	91.86	11.96
E69	9.42	31.24	42.9 (3.5)	48.18	11.53

* For the SLP_{MLC} calculation the slope was calculated according to the modified law of cooling. The adiabatic curve was reconstructed and linearly fitted. The R-squared error had in all cases a value of 0.99.The slope of the linearly fitted line was used for the calculation of SLP, thus it can be assumed that the calculated SLP values presented in Table 7 were a good estimation of the actual SLP values.

4.6. Parameters affecting the heating performance of Pd – SPIONs dispersed in hexane

4.6.1. Size

Based on the LRT model for a certain material there is a critical size which yields enhanced heating performance (see section 2.5.1). Values below or above that size lead to reduced heating rates, thus in thermal therapy it is important that the dimensions of the synthesized particles fall into this regime that causes high SLP values. From the obtained results can be seen that the samples of Group A related with high heating rates had a size of approximately 15 – 17 nm. On the other hand, the larger sizes of Group B resulted in a decrease in SLP values. Thus, for the Pd – IONPS that were tested, it seems that this critical size varies around 15 – 17 nm. However, this should be further investigated and more experiments should be carried out. More specifically, in order to estimate what would be the critical size related with elevated temperatures, for each of sample different sizes should be synthesized and the SLP values they cause during AMF exposure should be calculated in order to construct an SLP – size graph. This would verify whether the size range mentioned previously actually leads to the higher SLP values and thus enhanced heating performance.

4.6.2. Polydispersity

As mentioned in the previous paragraph sizes of approximately 15 – 17 nm (critical size) caused high SLP values. In order to get high heating rates, it is important for a sample to contain particles of sizes that match this critical value, since sizes above or below that value result in lower SLP values. The samples E47 and E56 contained particles of a larger sizes than the critical value which explained their poor heating performance compared to Group A samples. Based on TEM images Group B samples were polydispersed (see section 4.1), and contained even larger particles of 50 nm size. These larger particles further hindered the heating performance of the samples leading to lower SLP values. On the other hand, the samples E63, E68 and E69 were monodispersed containing particles that matched with the critical size and thus presented high SLP values.

4.6.3. Aggregation state

The aggregation and subsequent sedimentation of samples also affected their heating performance. As mentioned previously, in order to estimate whether any sedimentation took place during the heating experiments, two temperature channels were used, one at the center of the sample (T_A) and one at the side and bottom of the vial (T_B). Whenever $T_B > T_A$ there was an indication that precipitation occurred. As an example, in Fig. 34(a) T_A was higher than T_B during one minute of AMF exposure so no precipitation occurred during that experiment, in contrast with Fig. 34(b) in which particles had clearly precipitated.

Aggregation can result in the formation of nanoclusters and even macroclusters, a fact that can hinder the heating efficiency of a sample. Therefore, all samples were vortexed and sonicated before the heating measurements in order to reduce any aggregation. However, the two temperature channels indicated that the samples of Group B had the tendency to aggregate and precipitated soon after the sonication, which might be another reason that explains their low SLP values. On the other hand, for the samples of Group A, T_A and T_B indicated no precipitation, with the particles remaining in solution almost until the end of all experiments (all frequencies and magnitudes combinations were tested as mentioned in section 3.4.1), which provides further evidence of their increased heating capabilities.

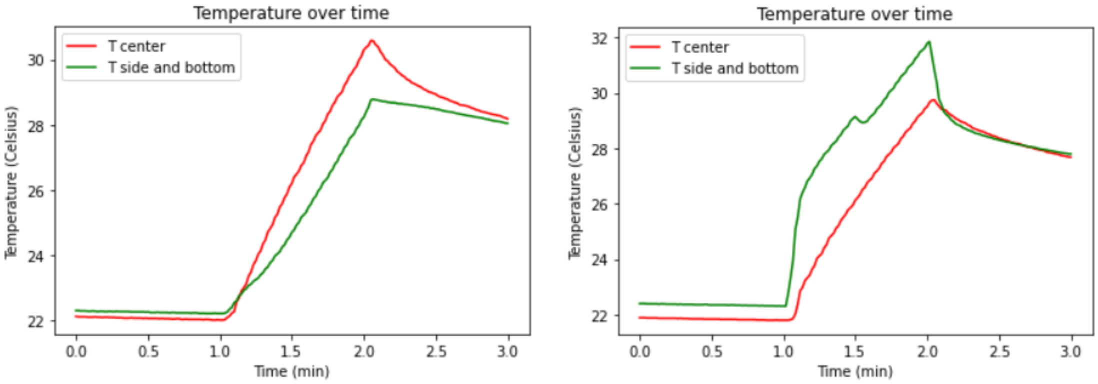

(a) (b)

Fig. 34: Temperature profile over time. In (a) $T_A > T_B$ during AMF exposure – no precipitation, (b) $T_B > T_A$ during exposure – precipitation occurred

4.6.4. Morphology

Particle morphology is another property that affects a sample's heating capability. Based on literature, cubic shapes are correlated with higher heating efficiency rather than spherical shapes due to their increased shape anisotropy. Sample E68 consisted of cubic particles, therefore presented yet another property that was related with high heating rates. Samples E63 and E69 were made of spherical particles, which might be a reason for their lower SLP values. It should be mentioned that even though the sample E47 consisted of cubic nanoparticles its heating capability was rather low. Since heating performance is related with many parameters, the polydispersity, the large size as well as the precipitation that occurred, probably were responsible for its low performance.

4.6.5. Magnetization

Saturation magnetization is another property that can affect the heating performance since according to the LRT model the SLP depends linearly to magnetization. The samples of Group B had relatively small magnetizations compared to the ones of Group A. For all the reasons described above and due to low magnetization, Group B did not present high heating performance in contrast to Group A.

It is noteworthy that even though the E68 sample had the lowest magnetization value in Group A, it was the sample with the highest SLP value, whereas E69 sample having the highest magnetization, presented the lowest SAR in the group. The opposite would be expected, since according to the LRT model the heating rate of a sample dependent to its magnetization. In other words, higher magnetization is expected to lead to higher heating rate. But this was not the case for the samples of Group A. An explanation for this lies in the shape anisotropy differences that the samples presented. According to Khushid et al.[77] optimization of shape anisotropy can lead to particles presenting higher SLP values regardless of their saturation magnetization. For example, cubic IONPs tested by this group with higher shape anisotropy but lower saturation magnetization were shown to have a higher heating efficiency compared to their spherical counterparts, 200 W/g compared to 135 W/g. This might be the case for the particles of Group A as well. The E68 sample, even though it presented the lowest magnetization, it consisted of cubic particles. Cubic particles have higher shape anisotropy compared to spherical particles (sample E63 and E69). Therefore, even though sample E69 presented higher magnetization than the E68 sample, the higher shape anisotropy of the E68 attributed to the cubic shape lead to better heating performance.

4.7. Heating performance of Pd - SPIONs dispersed in water

In order to develop samples for MRI – guided MNH it was crucial that the samples would first be efficient as heating agents and then they would be tested as T_2 contrast agents. In order to perform NMR experiments, the nanoparticles had to be transferred from hexane to water, since the aspect that determines a good T_2 CA is its ability to diffuse water protons along the inhomogeneous magnetic field that creates. Since human cells consist of mainly water it would be useful to test the contrast enhancing performance of the Group A samples in water. Post synthesis, the nanoparticles were coated with a combination of oleic acid and oleylamine, both previously mentioned surfactants being hydrophobic in nature, therefore making the nanoparticles dispersible in organic solvents only - like hexane. In order to enable the transfer of the nanoparticles to water, a surfactant exchange step was initially performed, interchanging the oleic acid/oleylamine with DMSA for sample E68. Apart from DMSA, another trial in making the nanoparticles water-dispersible was performed by encapsulation of all samples in group A (E63, E68, E69) with DSPE-PEG_{2000} COOH.

Before testing the contrast enhancing performance, heating measurements were performed to assess the heating capability of the samples this time in water. However, only the sample E68 coated with DMSA was tested since due to maintenance issues further experiments with MagneTherm^{TM} were not possible. The results are shown in Fig. 35. The temperature profile over time is shown for three time intervals: before AMF exposure (0 – 1 min), during AMF exposure (1 – 2 min) and after exposure (2 – 3 min). During the first seconds of exposure (1 – 1.5 min) the temperature T_A at the center of the bottle remained unchanged. This probably indicated that there were no particles present at the center of the sample and all of them were concentrated at the bottom of the cuvette. The fact that the temperature T_B at the bottom was increasing since the first moments of exposure supports this argument. At 1.5 min and until the end of AMF exposure T_A was increasing. This can be attributed to heat diffusion or convection from the lower to the upper parts of the sample. In more detail, heat diffuses from areas of higher temperature to areas of lower temperature. Since T_B was larger than T_A during the first moments of AMF exposure, it would be expected that heat was diffusing to the upper layers of the sample and caused T_A to increase. Another possible explanation can be particle convection. Particle movement due to temperature differences within the sample might have caused nanoparticles to migrate at the center of the sample where the temperature was lower. Once settled at the center, the particles started heating because of exposure to the AMF.

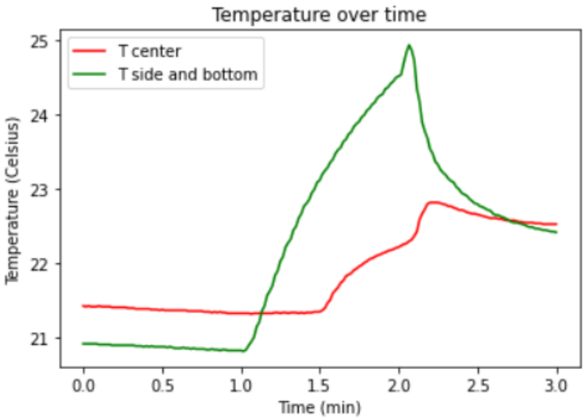

Fig. 35: Temperature profile over time for the E68 sample coated with DMSA in water solution

By comparing the heating performance of the E68 DMSA coated sample in water with the E68 oleic acid coated in hexane, it can be concluded that the temperature increase and the maximum temperature reached during exposure were dramatically decreased, from 17.34 °C to 3.69 °C and from 39.26 °C to 24.52 °C, respectively. This can be due to several facts. First of all, one of the main heating mechanisms in MNH is Brownian relaxation. The characteristic Brownian relaxation time is depended on the viscosity of the fluid that the particles are in suspension. The viscosity of hexane is $2.94 \cdot 10^{-4}$ Pa·s, whereas of water it is 8.90 ·

10^{-4} Pa·s. The fact that the viscosity of water is three times higher than hexane's, caused particles to physically rotate due to the applied AMF with more difficulty in water than in hexane. Thus, less friction was created and less heat was generated. Another reason can be attributed to the fact that the exchange of surfactant lead to reduced saturation magnetization from 60.53 emu/g to 35 emu/g, as can be seen in Fig. 36. The encapsulation of the oleic acid/oleylamine coated sample with a DMSA surfactant increased the coating thickness leading to more pronounce spin canting on the surface of the particles, which resulted in lower saturation magnetization. According to the LRT model SLP varies linearly with magnetization, therefore a decrease of the latter would result in less heat generated.

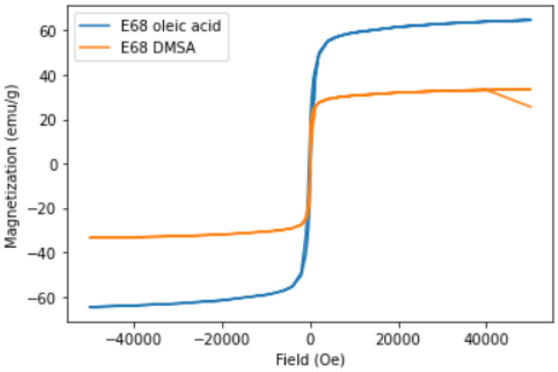

Fig. 36: Hysteresis loops for the sample E68 for two different surfactants

Another reason for the lower heating performance could be that the addition of the DMSA did not manage to sufficiently supress the aggregation of the particles leading to cluster formation, which is verified by the fact that most of the particles occupied the lower parts of the vial, as previously mentioned.

A first attempt to tackle the agglomeration was to add 1 ml of 0.5% xanthan solution to the E68 sample of 5 mg/ml. Xanthan is a polysaccharide which increased the viscosity of the sample, preventing particles from aggregating. The new sample (2.5 mg/ml) was again measured for its heating performance. With the new sample, T_A was slightly increasing since the beginning of the AMF exposure, indicating that there were some particles present at the center of the sample (Fig. 38). However, the temperature at the bottom of the sample was still increasing with a higher rate than the one at the center according to Fig. 37. Thus, particles were still sedimenting even after mixing with xanthan solution.

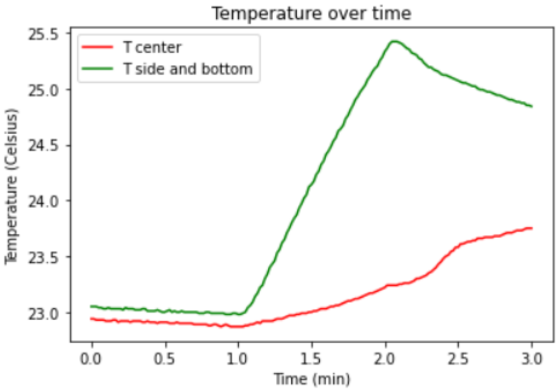

Figure 37: Temperature profile of E68 DMSA coated sample in water and xanthan solution

To eliminate the sedimentation problem an alternative measure was taken. Agar solution (2%) was added to the E68 sample with water and xanthan. From Fig. 38 can be seen that the temperature at the center of the sample started increasing since the beginning of the AMF exposure and it was higher than the one at the bottom, indicating that the particles were homogeneously dispersed in the solution and no aggregation occurred. However, since more water was added the sample's concentration became lower (1.25 mg per ml) leading to less heat being generated.

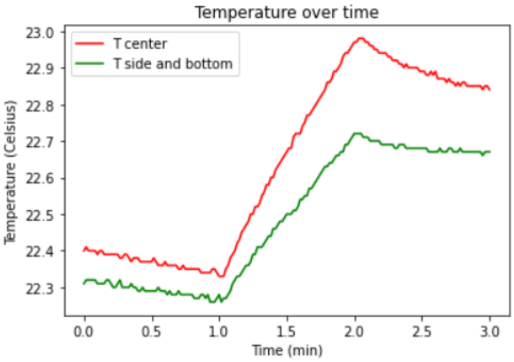

Figure 38: Temperature profile of E68 DMSA coated sample in water – xanthan – agar solution

The E68 sample was compared with the Hypermag commercial nanoparticles in order to further determine what would be the optimum properties that particles should have for enhanced heating performance. The commercial particles presented a temperature increase of 8.63 ^{o}C and reached a maximum temperature of 31.43 ^{o}C during one minute of AMF exposure at 345 kHz and 19 mT (Fig. 39a). This is much higher than the maximum temperature that sample E68 in water – agar – xanthan reached (Fig. 39a). This was however expected since the concentration of commercial particles used was 5 mg/ml in water whereas for the E68 sample it was approximately 1.25 mg/ml in water – xanthan – agar solution. Heating performance depends on concentration therefore the lower concertation of E68 resulted in lower temperatures.

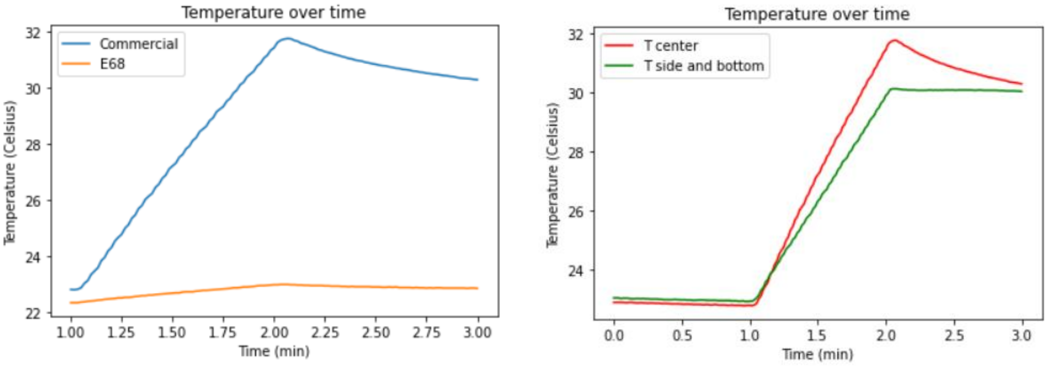

(a) (b)

Figure 39: (a) Temperature profile of E68 DMSA coated sample in water – xanthan – agar solution and commercial Hypermag coated with DMSA in water

According to Table 7, when dispersed in hexane Group A samples reached higher temperatures under AMF exposure than the commercial particles did in water (31.43 ^{o}C). However, such comparisons are not valid, since the solvents were different in each case. In order to make fair comparisons, the Group A samples coated with DSPE – PEG$_{2000}$ COOH and commercial particles of comparable concentrations and dispersed in the same solvent (water) should be tested with MagneTherm^{TM}, since the functionalization with DMSA was not proper.

Since the magnetization of the synthesized particles coated with DSPE – PEG$_{2000}$ COOH was reduced compared with the ones coated with oleic acid/oleylamine (see section 4.4), it would be expected that less heat would be generated in water compared with the particles tested in hexane, since SLP depends on magnetization. Moreover, the higher viscosity of the water would also hinder the heating performance. Therefore, even though the heating performance of the synthesized samples dispersed in hexane was better than the commercial sample's performance in water, this does not necessarily make the synthesized particles better heating agents. A comparison of Group A samples and commercial particles both dispersed in the same solvent (water) should be made in order to determine which samples have the best heating performance.

Regarding physical and magnetic properties, the size of the commercial particles was almost the same as the ones of Group A samples and the commercial sample was monodispersed as the E63, E68 and E69. The commercial particles also showed no sedimentation during the heating experiments as can be seen in Fig. 39b, which is another that feature that have in common with the synthesized particles. However, they presented higher magnetization compared to the Group A samples (see section 4.4), which might cause higher SLP values than the synthesized particles.

Regarding concentration, the commercial particles were diluted and tested with the heating device in order to estimate what would be the minimum concentration that would cause a considerable heating. Different concentrations were used: 5, 4, 3, 2, 1 mg/ml and 0.5, 0.4, 0.3, 0.2 and 0.1 mg/ml respectively. The results are presented in Fig. 40 and Table 8. From the results it can be seen that the minimum concentration that can cause considerable heating under AMF exposure is 0.5 mg/ml. Below this concentration the temperature increase is less than 1 ^{o}C over one minute of AMF exposure. Therefore, for hyperthermia experiments samples with a concentration above 0.5 mg/ml are needed.

Table 8: Heating experiment results of commercial particles at different concentrations. The uncertainty in temperature measurement is 0.01 ^{o}C taken my multiple measurements under the same conditions

Concentration (mg/ml)	Maximum T (^{o}C)	T increase (^{o}C)
5	31.49	8.25
4	30.56	7.25
3	29.48	6.05
2	26.96	4.97
1	27.2	3.93
0.5	26.41	2.75
0.4	22.32	0.88
0.3	23.15	0.75
0.2	22.02	0.75
0.1	22.16	0.63

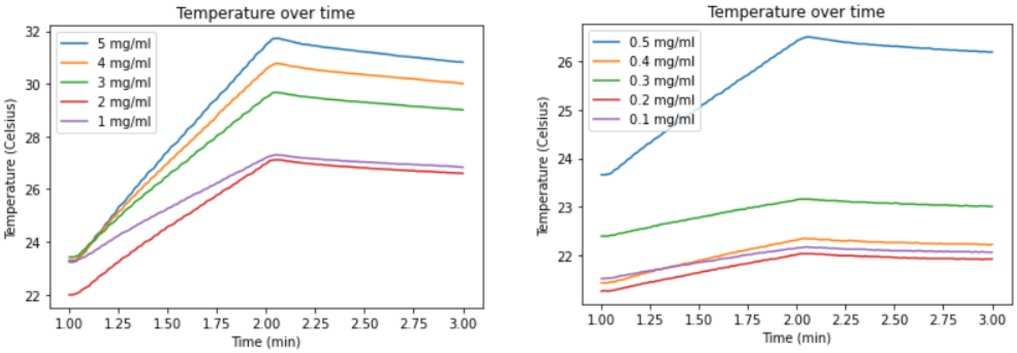

(a) (b)

Figure 40: Temperature profile over time for different concetrations of commercial particles, (a) in the range 1 – 5 mg/ml and (b) in the range 0.5 – 0.1 mg/ml

4.8. Contrast enhancing performance of Pd - SPIONs dispersed in water

The results of the relaxometry studies with NMR are presented in Table 9. It can be seen that E68 had the highest R_2 relaxation rate among the synthesized samples. In order to evaluate which particle properties were related with the high relaxivity performance, the influence of structural and magnetic motifs on the contrast enhancing performance was investigated.

Table 9: Relaxation rates and R_2/R_1 ratio for the three Pd – SPION samples coated with DSPE – PEG_{2000} COOH and commercial particles coated with DMSA while dispersed in water

Sample	R_1 (s^{-1})	R_2 (s^{-1}) *
E63	0.6072	9.926
E68	0.7942	15.10
E69	0.6086	10.51
Commercial	7.156	30.26

From literature it is known that saturation magnetization greatly influences transverse relaxation rate since $R_2 \propto \mu_c^2$. From Table 5 can be seen that E68 had the highest magnetization at 238 K compared to E63 and E69. A large magnetization creates stronger field gradients applied by the particles. Because of this, the dephasing of the water protons that diffuse through the particle environment is more pronounced, causing the shortening of water protons' T_2 times and therefore the increase of r_2 relaxivities. The higher magnetization of E68 caused more pronounced dephasing to water protons which lead to higher transverse relaxation rate.

Size is another property that affects transverse relaxation rate. In general, larger sizes result in higher magnetization values due to less significant spin canting effects and thus higher transverse relaxivities. From Table 4 can be seen that sample E63 consists of particles larger in size in comparison with sample E68. From the relaxivity data, however, can be seen that E68 presents higher transverse relaxation rate that E63, which is not in agreement with the literature. Size, however, is not the only property that affects relaxivity.

Shape anisotropy also influences the transverse relaxivity of nanoparticles. A change in shape of particles affects the effective anisotropy. Cubic particles having larger shape anisotropy than spherical particles can and lead to higher relaxivities. From Table 4 can be seen that E68 is comprised of cubic particles in contrast with the other two samples that consist of spherical particles. The increase anisotropy attributed to the cubic shape of E68 resulted in higher transverse relaxation rate. Therefore, even though E68 particles had smaller size than E63, their increased shape anisotropy attributed to their cubic shape led to higher transverse relaxation rate. Moreover, because spheres have more curved surface than cubes, spin canting can be more pronounced. Spin canting leads to lower magnetization and thus lower transverse relaxivity.

In comparison with the commercial sample the E68 had a lower transverse relaxation rate. Even though sample E68 consisted of cubic particles of comparable sizes with the spherical Hypermag particles, its saturation magnetization value was lower. This can explain the higher relaxivity rate of the commercial particles. In general, cubic morphology leads to higher shape and thus effective anisotropy and less significant spin canting effect than spherical shape. Thus, it would be expected that the E68 would present higher magnetization. However, saturation magnetization depends also on the magnetocrystalline anisotropy. The reason for the higher magnetizations of the commercial particles might possible lie in the fact that their crystal structure resulted in higher magnetocrystalline anisotropy compared to the E68 sample and thus higher magnetization values. Further experiments with Mossbauer spectroscopy could reveal information about the crystal structure of the samples.

* The relaxation rates were calculated by exponentially fitting the experimental data obtained from a CPMG sequence. The fitting error was for all cases less than 0.2, which signified that the calculated relaxivity rate values presented in Table 9 were a good estimation of the actual values

4.9. MRI and CT studies with commercial SPIONs

Regarding the application of MRI – guided TA with ^{103}Pd – SPIONs, the particles will be intratumorally injected into a patient. An MRI scan will be performed post injection in order to determine when particles will start diffusing into the tumor tissue. At that point the thermotherapy will be initiated and the particles will be subjected to AMFs. After the treatment MRI will be again used to monitor the effect of the treatment. The visualization of the particles within the tumor would give information that can be used for dosimetry purposes. Once the nanoparticles start diffusing around the tumor, different concentrations would emerge in the tumor region and even throughout the body. From literature it is know that the relaxivity of water protons increases with the contrast agent's concentration, which gives rise to the question of whether the MRI quantification of areas with different concentrations within the patient would be possible.

From the NMR experiments it was determined that even for low particle concentrations very fast relaxation rates of protons occurred and thus the samples had to be diluted multiple times in order to calculate the transverse relaxivity rates. It should be noted to this point that the minimum concentration of commercial particles that caused considerable heating was 0.5 mg/ml. Therefore, the concentration of particles injected into the patient should be considerably higher. It would be therefore expected that since the relaxivity is high even for the low concentrations, the regions in which particles would be present would appear dark in a T_2 weighted image of breast. Breast appears bright in such images therefore information about the location of the nanoparticles should be possible. However due to the very fast relaxation it would be expected that differentiation between different concentrations would be difficult.

To test this notion samples of commercial SPIONs provided by Hypermag, with different concentrations of 2, 0.5 and 0.2 mg/ml in agar solution (0.01 mg/ml) were prepared and used in MRI phantom studies.

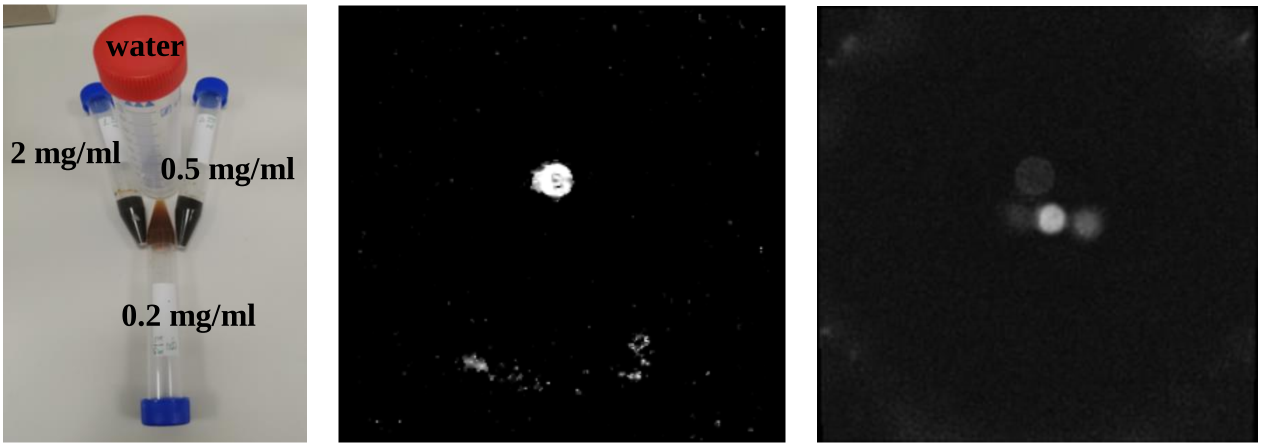

(a) (b) (c)

Figure 41: (a) Phantom used in MRI studies, (b) scan obtained for the IDEAL IQ sequence, (c) scan obtained by the ZTE sequence

For the MRI studies an R_2^* IDEAL IQ Multi Echo Gradient Echo sequence was used. From the MRI results in Fig. 41b can be seen that the reference signal from water was bright, whereas none of the commercial particle samples produced any signal. Instead they appeared dark as it was first assumed. The relaxation however, was so fast that quantification of relaxivities was impossible. Because of this, in an attempt to quantify the relaxivity from different concentrations, a Zero Echo Time Sequence was used. This sequence enabled very fast echo times, close to zero. For this study an echo time of 0.02 msec was used. From the results in Fig. 41c can be seen that the sample with the lowest concentration created some signal in contrast with the other two samples, which indicates that the relaxation they caused was so fast that even with a very short echo time no signal could be produced. Again the relaxivities could not be quantified.

From the above can be seen that SPIONs could be used as CAs in T_2 weighted images since the fast relaxivity they create in water protons would make the regions they are present to appear darker in a bright breast image. Therefore, contrast can be created and information about the location of the particles could be obtained. However, quantification was not possible. It could be assumed that once the particles diffuse in the tumour tissue and very low concentrations arise, probanly quantification might be possible. To further investigate this, further quantitative MRI studies using phantoms with multiple concentrations (even lower ones than the ones used in this study) might provide information regarding whether MRI quantification would actually be possible.

Since quantification of relaxivities was not possible with MRI with the given concentrations, a different approach was attempted in order to determine whether any quantitive infromation about particle concentration could be obtained. Since the commercial particles were made of iron (Z = 26) an X – ray beam would be attenuated when passed through a sample. Different concentrations of iron in the same volume should cause different attenuations of the X – ray beam and thus result in different Hounsfield Units (HU). To this regard, different concentrations of commercial nanoparticles in water were prepared and scanned with a CT scanner. It was expected that they would result in different HU and thus it would be possible to differentiate between different concentrations.

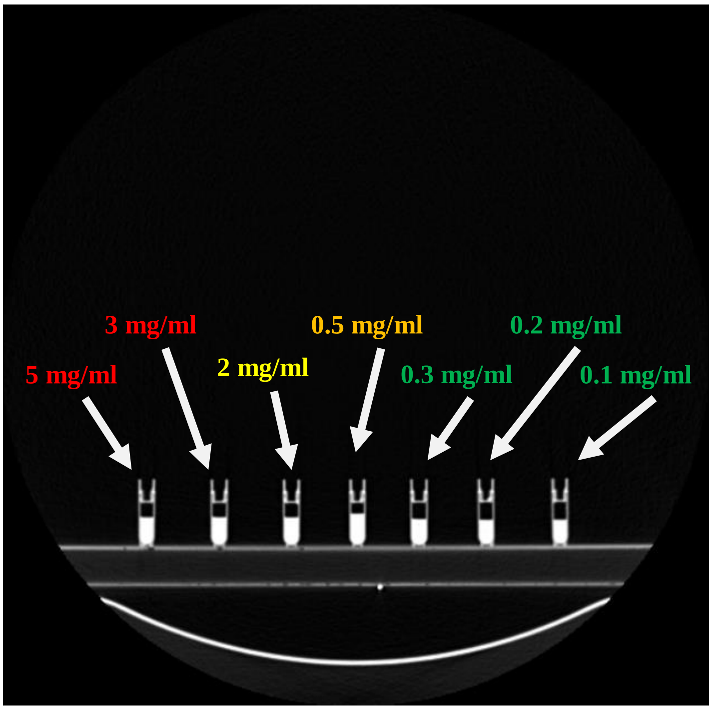

Fig. 43: CT scan of commercial particles with different concentrations

The results of the CT study are depicted in Fig. 43 and Fig. 44. In Fig. 44 can be seen that even though there was an increase in HU with increasing concentration, the uncertainty was too high to be able to extract any conclusions about quantification. In order to determine whether the different samples could differentiate, statistical analysis was performed. Since for each sample the mean and standard deviation of the HU were calculated, a Z – test was conducted in order to determine whether a sample was same or different from another, based on the mean HU obtained from the CT scan.

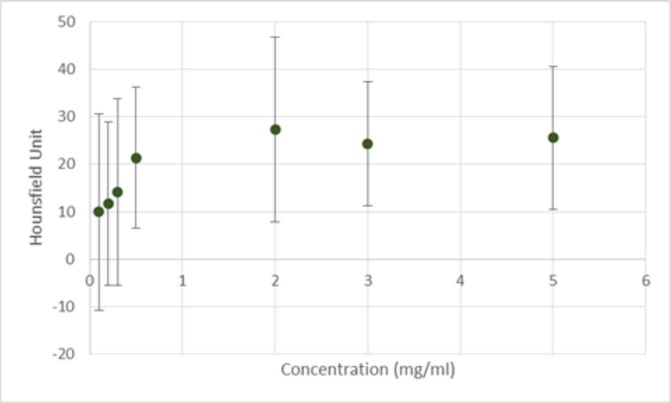

Fig. 44: Mean HU vs sample concentration. The uncertainty (standard deviation) is too high to be able to extract any conclusions about quantification

The purpose of the Z – test is to determine whether two distributions (with a mean and standard deviation value) are significantly different from each other. From Fig. 44 can be seen that the HU of each sample might possibly overlap with one another due to the high uncertainty. In order to compare two distributions the Zeta statistic is calculated

$$Z = \frac{X_1 - X_2}{\sqrt{\frac{s_1^2}{N_1} + \frac{s_2^2}{N_2}}} \qquad (14)$$

where $X_{1,2}$ is the mean value, $S_{1,2}$ is the standard deviation and $N_{1,2}$ the number of measurements of distribution 1 and 2, respectively. Based on the value of the Z – statistic it can be concluded whether two distributions are statistically different from each other. More specifically:

- If $Z < 2$, the samples are the same
- If $2 < Z < 2.5$, the samples are marginally different
- If $2.5 < Z < 3$, the samples are significantly different
- If $Z > 3$, the samples are highly significantly different

Using the calculated mean and standard deviation of the HU of each sample, the Z statistic was calculated for different combinations of samples with different concentrations. The results are presented in Table 10.

Table 10: Z – statistic values for multiple combinations of samples with different concentrations

Combinations of concentration samples (mg/ml)	Z - statistic
5 with 3	0
3 with 2	2.8
0.3 with 0.1	1.4
0.2 with 0.1	1.0
2 with 0.5	2.7
2 with 0.3	7.7
0.5 with 0.3	5.6

From the results can be seen that the samples of concentration 5, 3 mg/ml were statistically the same, therefore they gave identical HU in a CT scan. The samples 0.3, 0.2 and 0.1 mg/ml were also identical between them, therefore in a CT scan those would not appear different. However, those two groups of concentrations were highly significantly different according to Table 10, which meant that they resulted in different HU and thus they could appear different in a CT scan. The 2 mg/ml and the 0.5 mg/ml could also be differentiated from the rest of concentrations based on the zeta statistic.

5 Conclusion

The heating and T_2 contrast enhancing performance of multiples Pd – SPION samples and commercial particles, for thermotherapy and MRI, respectively, were investigated. Whether a sample was considered a good/bad heating and contrast agent was highly dependent the physical and magnetic properties of the particles it consisted of. In order to draw conclusions on which sample presented the best performance, all samples were fully characterized and tested as heating and contrast agents. The parameters leading to an enhanced performance were investigated and determined.

Six different Pd – SPION samples coated with oleic acid and dispersed in hexane were used in the heating measurements. It was concluded that the E68 presented the best heating performance among the rest of the samples. The sample consisted of particles of 15.47 ± 2.07 nm in size, which appeared to be the critical size that yielded the highest SLP value. The other samples had sizes that were larger or smaller than this critical size, thus presented lower heating rates. Moreover, the E68 sample was monodispersed, thus it did not consist of particles with bigger or smaller sizes that would lead to lower SLP values. According to the heating experiments, no aggregation and subsequent sedimentation was observed which provides further evidence for the sample's increased heating capability. The cubic shape of the nanoparticles was another parameter that lead to enhanced heating performance, due to high shape anisotropy and less pronounced spin canting effect in comparison with spherical particles. Shape anisotropy is an important parameter since its optimization can lead to particles presenting higher SLP values regardless of their saturation magnetization. E68 presented lower magnetization compared with E63 and E69, however the higher shape anisotropy of the E68 due to their cubic shape lead to better heating performance.

Further heating experiments of the synthesized particles coated with DSPE – PEG_{2000} COOH should be made in order to compare the heating performance of the synthesized and commercial particles. Regarding their physical properties, the size of the commercial particles was comparable with the ones of Group A samples and the commercial sample was monodispersed as the E63, E68 and E69. The commercial particles also did not sedimentate during the heating experiments which is another that feature that have in common with the synthesized particles. However, Hypermag particles presented higher magnetization compared to the Group A samples.

For the NMR experiments the samples that presented the best heating performance were coated with DSPE – PEG_{2000} COOH and were dispersed in water. Again it was concluded that E68 presented the best contrast enhancing performance. Due to change of surfactant the saturation magnetization of all samples decreased in comparison with the oleic acid/oleylamine coated samples, due to increased coating thickness leading to more pronounce spin canting effect. The E68 sample presented the higher saturation magnetization among the rest of the samples which lead to stronger field gradients applied by the nanoparticles. Because of this, the dephasing of the water protons that diffused through the Pd – SPIONs' environment was more pronounced, causing the shortening of protons' T_2 times and therefore the increase of R_2 relaxation rates. Moreover, E68 was comprised of cubic particles in contrast with the other two samples that consisted of spherical particles. The increase in anisotropy of E68 resulted in higher transverse relaxation rate. No aggregation and subsequent sedimentation was observed which is considered as another reason for the enhanced performance. In comparison with the commercial sample the E68 had a lower transverse relaxation rate. The saturation magnetization value of the cubic particles of sample E68 was lower than the commercial sample's one made of spherical particles. The reason for the higher magnetizations of the commercial particles might possible lie in the fact that their crystal structure resulted in higher magnetocrystalline anisotropy compared to the E68 sample and thus higher magnetization values. This might possibly explain the higher relaxation rate of the commercial sample.

The very fast T_2 relaxation of water proton that the commercial particles caused in agar solutions, made the quantification of relaxivity with MRI impossible. Therefore, information about the different concentrations could not be obtained. However, due to the very fast relaxation they induced, the particle could produce contrast and thus would provide information about their location in a breast T_2 – weighed image. Since MRI quantification was impossible, CT quantification was investigated. Samples of different concentrations resulted in different HU based on the zeta statistical analysis and could be thus differentiated in a CT scan.

6 Future Research

Six different samples coated with oleic acid/oleylamine and dispersed in hexane were tested for their heating performance with MagneTherm^{TM}. The samples of Group A (E63, E68 and E69) presented the highest heating rates. In order to transfer them to water the samples were encapsuled with DSPE – PEG_{2000} COOH. However, further heating experiments were not possible. It would be therefore of interest to compare the heating performance of the Group A samples coated with DSPE – PEG_{2000} COOH with the commercial particles and determine whether they are better/worse heating agents.

During the heating measurements in hexane, samples were exposed to AMFs for one minute. This was done since the interest in this thesis was placed on the characterization of the samples and the goal was to determine which samples could heat up under AMF exposure and which could not and what were the parameters related to their performance. It would be of interest to determine whether the synthesized particles could reach thermal ablation temperatures and under what conditions (i.e. how long will it take for the particles to exceed 50°C, what concentration will be needed, what will be the right combination of AMF frequency and magnitude etc.) For those further heating experiment are needed.

Regarding the MRI phantom studies, it would be of interest to perform studies with the synthesized particles of Group A. Since quantification of different concentrations was not possible, it would be of interest to perform studies with phantoms of multiple different concentrations and determine whether MRI quantification would actually be possible.

Bibliography

1. Kaczmarek, K., Mrówczyński, R., Hornowski, T., Bielas, R. & Józefczak, A. The effect of tissue-mimicking phantom compressibility on magnetic hyperthermia. *Nanomaterials* **9**, (2019).
2. Pucci, C., Martinelli, C. & Ciofani, G. Innovative approaches for cancer treatment: Current perspectives and new challenges. *Ecancermedicalscience* **13**, 1–26 (2019).
3. Horsman, M. R. & Overgaard, J. Hyperthermia: a Potent Enhancer of Radiotherapy. *Clin. Oncol.* **19**, 418–426 (2007).
4. Kaur, P., Aliru, M. L., Chadha, A. S., Asea, A. & Krishnan, S. Hyperthermia using nanoparticles - Promises and pitfalls. *Int. J. Hyperth.* **32**, 76–88 (2016).
5. Dennis, C. L. & Ivkov, R. Physics of heat generation using magnetic nanoparticles for hyperthermia. *Int. J. Hyperth.* **29**, 715–729 (2013).
6. Giustini, A. J. *et al.* Nano Life. *Nano Life* **1**, 17–32 (2010).
7. Nijhawan, G., Nijhawan, S. S. & Sethi, M. Hyperthermia Treatments. *Noble Met. Oxide Hybrid Nanoparticles Fundam. Appl.* 241–263 (2018) doi:10.1016/B978-0-12-814134-2.00012-7.
8. Halperin, E. *et al.* Chapter 31 Hyperthermia as a Treatment Modality The BIOLOGY of Hyperthermia Definition of Hyperthermia. *Perez Brady's Princ. Pract. Radiat. Oncol.* 1–35 (2013).
9. Abbas, Z. & RehmanS. An Overview of Cancer Treatment Modalities. *Neoplasm, InTech* (2018).
10. van Maaren, M. C., de Munck, L., de Bock, G. H., Jobsen, J. J., van Dalen, T., Linn, S. C., Poortmans, P., Strobbe, L. J. A. & Siesling, S. 10 year survival after breast-conserving surgery plus radiotherapy compared with mastectomy in early breast cancer in the Netherlands: a population-based studyNo Title. *Lancet Oncol.* **17**, 1158–1170.
11. Taylor, C. W. & Kirby, A. M. Cardiac Side-effects From Breast Cancer Radiotherapy. *Clin. Oncol. (R. Coll. Radiol).* **27**, 621–629 (2015).
12. GILCHRIST, R. K. *et al.* Selective inductive heating of lymph nodes. *Ann. Surg.* **146**, 596–606 (1957).
13. Pignol, J.-P., Rakovitch, E., Keller, B. M., Sankreacha, R. & Chartier, C. Tolerance and acceptance results of a palladium-103 permanent breast seed implant Phase I/II study. *Int. J. Radiat. Oncol. Biol. Phys.* **73**, 1482–1488 (2009).
14. Wabler, M. *et al.* Magnetic resonance imaging contrast of iron oxide nanoparticles developed for hyperthermia is dominated by iron content. *Int. J. Hyperth.* **30**, 192–200 (2014).
15. MagneTherm Consumables. http://www.nanotherics.com/magnetherm-consumables/.
16. Estelrich, J., Sánchez-Martín, M. J. & Busquets, M. A. Nanoparticles in magnetic resonance imaging: From simple to dual contrast agents. *Int. J. Nanomedicine* **10**, 1727–1741 (2015).
17. Sun, C., Lee, J. S. H. & Zhang, M. Magnetic nanoparticles in MR imaging and drug delivery. *Adv. Drug Deliv. Rev.* **60**, 1252–1265 (2008).
18. Rosensweig, R. E. Heating magnetic fluid with alternating magnetic field. *J. Magn. Magn. Mater.* **252**, 370–374 (2002).
19. Makridis, A., Curto, S., van Rhoon, G. C., Samaras, T. & Angelakeris, M. A standardisation protocol for accurate evaluation of specific loss power in magnetic hyperthermia. *J. Phys. D. Appl. Phys.* **52**, 255001 (2019).
20. Dutz, S. & Hergt, R. Magnetic nanoparticle heating and heat transfer on a microscale: Basic principles, realities and physical limitations of hyperthermia for tumour therapy. *Int. J. Hyperth.* **29**, 790–800 (2013).
21. Blanco-Andujar, C. *et al.* Design of iron oxide-based nanoparticles for MRI and magnetic hyperthermia. *Nanomedicine* **11**, 1889–1910 (2016).
22. Gahrouei, Z. E., Labbaf, S. & Kermanpur, A. Cobalt doped magnetite nanoparticles: Synthesis, characterization, optimization and suitability evaluations for magnetic hyperthermia applications. *Phys. E Low-Dimensional Syst. Nanostructures* **116**, 113759 (2020).
23. Simeonidis, K. *et al.* Fe-based nanoparticles as tunable magnetic particle hyperthermia agents. *J. Appl.*

Phys. **114**, (2013).

24. Chalkidou, A. *et al.* In vitro application of Fe/MgO nanoparticles as magnetically mediated hyperthermia agents for cancer treatment. *J. Magn. Magn. Mater.* **323**, 775–780 (2011).
25. Papadopoulos, C. *et al.* Magnetic fluid hyperthermia simulations in evaluation of SAR calculation methods. *Phys. Medica* **71**, 39–52 (2020).
26. Wildeboer, R. R., Southern, P. & Pankhurst, Q. A. On the reliable measurement of specific absorption rates and intrinsic loss parameters in magnetic hyperthermia materials. *J. Phys. D. Appl. Phys.* **47**, (2014).
27. Lanier, O. L. *et al.* Evaluation of magnetic nanoparticles for magnetic fluid hyperthermia. *Int. J. Hyperth.* **36**, 687–701 (2019).
28. Gonzales-Weimuller, M., Zeisberger, M. & Krishnan, K. M. Size-dependant heating rates of iron oxide nanoparticles for magnetic fluid hyperthermia. *J. Magn. Magn. Mater.* **321**, 1947–1950 (2009).
29. Abenojar, E. C., Wickramasinghe, S., Bas-Concepcion, J. & Samia, A. C. S. Structural effects on the magnetic hyperthermia properties of iron oxide nanoparticles. *Prog. Nat. Sci. Mater. Int.* **26**, 440–448 (2016).
30. Hergt, R. *et al.* Physical limits of hyperthermia using magnetite fine particles. *IEEE Trans. Magn.* **34**, 37453754 (1998).
31. Nemati, Z. *et al.* Enhanced Magnetic Hyperthermia in Iron Oxide Nano-Octopods: Size and Anisotropy Effects. *J. Phys. Chem. C* **120**, 8370–8379 (2016).
32. De La Presa, P. *et al.* Study of heating efficiency as a function of concentration, size, and applied field in γ-Fe2O3 nanoparticles. *J. Phys. Chem. C* **116**, 25602–25610 (2012).
33. Vreeland, E. C. *et al.* Enhanced Nanoparticle Size Control by Extending LaMer's Mechanism. *Chem. Mater.* **27**, 6059–6066 (2015).
34. Jiang, P. S., Tsai, H. Y., Drake, P., Wang, F. N. & Chiang, C. S. Gadolinium-doped iron oxide nanoparticles induced magnetic field hyperthermia combined with radiotherapy increases tumour response by vascular disruption and improved oxygenation. *Int. J. Hyperth.* **33**, 770–778 (2017).
35. Lee, J. H. *et al.* Exchange-coupled magnetic nanoparticles for efficient heat induction. *Nat. Nanotechnol.* **6**, 418–422 (2011).
36. Bauer, L. M., Situ, S. F., Griswold, M. A. & Samia, A. C. S. High-performance iron oxide nanoparticles for magnetic particle imaging-guided hyperthermia (hMPI). *Nanoscale* **8**, 12162–12169 (2016).
37. Jiles, D. Magnetic Materials. in *Introduction to Magnetism and Magnetic Materials* (ed. Jiles, D.) 89–109 (Boca Raton, 2015).
38. Jadhav, S. V., Nikam, D. S., Mali, S. S., Hong, C. K. & Pawar, S. H. The influence of coating on the structural, magnetic and colloidal properties of LSMO manganite and the heating mechanism for magnetic fluid hyperthermia application. *New J. Chem.* **38**, 3678–3687 (2014).
39. Yuan, Y. *et al.* Effect of surface modification on magnetization of iron oxide nanoparticle colloids. *Langmuir* **28**, 13051–13059 (2012).
40. Doan, B. T., Meme, S. & Beloeil, J. C. General Principles of MRI. *Chem. Contrast Agents Med. Magn. Reson. Imaging Second Ed.* 1–23 (2013) doi:10.1002/9781118503652.ch1.
41. Rabai, F. and Ramani, R. Magnetic Resonance Imaging: Anesthetic Implications. in *Essentials of Neuroanesthesia* 519–532 (Academic Press, 2017).
42. van Geuns, R.-J. M. *et al.* Basic principles of magnetic resonance imaging. *Prog. Cardiovasc. Dis.* **42**, 149–156 (1999).
43. Hornak, J. P. The Basics of MRI. http://www.cis.rit.edu/htbooks/mri/.%0D.
44. MRI: The Dance Of The Whirling Protons.
45. Elster, A. T2 (Spin-Spin) Relaxation. [online] Questions and Answers in MR.
46. Fonseca,] Gonçalves. Spin Echo Magnetic Resonance Imaging. in *Imaging and Radioanalytical Techniques in Interdisciplinary Research* (2013).
47. Huang, J., Zhong, X., Wang, L., Yang, L. & Mao, H. Improving the magnetic resonance imaging contrast and detection methods with engineered magnetic nanoparticles. *Theranostics* **2**, 86–102

(2012).
48. Shokrollahi, H. Contrast agents for MRI. *Mater. Sci. Eng. C* **33**, 4485–4497 (2013).
49. Bakhtiary, Z. *et al.* Targeted superparamagnetic iron oxide nanoparticles for early detection of cancer: Possibilities and challenges. *Nanomedicine Nanotechnology, Biol. Med.* **12**, 287–307 (2016).
50. Brooks, R. A., Moiny, F. & Gillis, P. On T2-shortening by weakly magnetized particles: The chemical exchange model. *Magn. Reson. Med.* **45**, 1014–1020 (2001).
51. Dadfar, S. M. *et al.* Size-isolation of superparamagnetic iron oxide nanoparticles improves MRI, MPI and hyperthermia performance. *J. Nanobiotechnology* **18**, 1–13 (2020).
52. Hirt, A. M., Kumari, M., Heinke, D. & Kraupner, A. Enhanced methods to estimate the efficiency of magnetic nanoparticles in imaging. *Molecules* **22**, 1–14 (2017).
53. Veiseh, O., Gunn, J. W. & Zhang, M. Design and fabrication of magnetic nanoparticles for targeted drug delivery and imaging. *Adv. Drug Deliv. Rev.* **62**, 284–304 (2010).
54. Pöselt, E. *et al.* Relaxivity optimization of a pegylated iron-oxide-based negative magnetic resonance contrast agent for T 2-weighted spin-echo imaging. *ACS Nano* **6**, 1619–1624 (2012).
55. Yoon, T.-J., Lee, H., Shao, H. & Weissleder, R. Highly magnetic core-shell nanoparticles with a unique magnetization mechanism. *Angew. Chem. Int. Ed. Engl.* **50**, 4663–4666 (2011).
56. Smolensky, E. D. *et al.* Scaling Laws at the Nano Size: The Effect of Particle Size and Shape on the Magnetism and Relaxivity of Iron Oxide Nanoparticle Contrast Agents. *J. Mater. Chem. B* **1**, 2818–2828 (2013).
57. Lee, N. *et al.* Magnetosome-like ferrimagnetic iron oxide nanocubes for highly sensitive MRI of single cells and transplanted pancreatic islets. *Proc. Natl. Acad. Sci. U. S. A.* **108**, 2662–2667 (2011).
58. Jun, Y.-W., Seo, J.-W. & Cheon, J. Nanoscaling laws of magnetic nanoparticles and their applicabilities in biomedical sciences. *Acc. Chem. Res.* **41**, 179–189 (2008).
59. Lartigue, L. *et al.* Cooperative organization in iron oxide multi-core nanoparticles potentiates their efficiency as heating mediators and MRI contrast agents. *ACS Nano* **6**, 10935–10949 (2012).
60. Zhao, Z. *et al.* Octapod iron oxide nanoparticles as high-performance T 2 contrast agents for magnetic resonance imaging. *Nat. Commun.* **4**, (2013).
61. Lee, J.-H. *et al.* Artificially engineered magnetic nanoparticles for ultra-sensitive molecular imaging. *Nat. Med.* **13**, 95–99 (2007).
62. Yang, H. *et al.* Water-soluble superparamagnetic manganese ferrite nanoparticles for magnetic resonance imaging. *Biomaterials* **31**, 3667–3673 (2010).
63. Jang, J. *et al.* Critical enhancements of MRI contrast and hyperthermic effects by dopant-controlled magnetic nanoparticles. *Angew. Chem. Int. Ed. Engl.* **48**, 1234–1238 (2009).
64. Wang, W. *et al.* Size and compositional effects on contrast efficiency of functionalized superparamagnetic nanoparticles at ultralow and ultrahigh magnetic fields. *J. Phys. Chem. C* **116**, 17880–17884 (2012).
65. De Montferrand, C. *et al.* Iron oxide nanoparticles with sizes, shapes and compositions resulting in different magnetization signatures as potential labels for multiparametric detection. *Acta Biomater.* **9**, 6150–6157 (2013).
66. Sensitive, H. *et al.* Supporting Information for Water-dispersible ferrimagnetic iron oxide nanocubes with extremely high r 2 relaxivity for highly sensitive in vivo MRI of tumors. *Nano Lett.* (2012).
67. Duan, H. *et al.* Reexamining the Effects of Particle Size and Surface Chemistry on the Magnetic Properties of Iron Oxide Nanocrystals: New Insights into Spin Disorder and Proton Relaxivity. *J. Phys. Chem. C* **112**, 8127–8131 (2008).
68. Tong, S., Hou, S., Zheng, Z., Zhou, J. & Bao, G. Coating optimization of superparamagnetic iron oxide nanoparticles for high T2 relaxivity. *Nano Lett.* **10**, 4607–4613 (2010).
69. LaConte, L. E. W. *et al.* Coating thickness of magnetic iron oxide nanoparticles affects R2 relaxivity. *J. Magn. Reson. Imaging* **26**, 1634—1641 (2007).
70. Pinho, S. L. C. *et al.* Relaxometric studies of γ-Fe 2 O 3 @SiO 2 core shell nanoparticles: When the coating matters. *J. Phys. Chem. C* **116**, 2285–2291 (2012).
71. Chen, H. *et al.* Preparation and control of the formation of single core and clustered nanoparticles for

biomedical applications using a versatile amphiphilic diblock copolymer. *Nano Res.* **3**, 852–862 (2010).

72. Ai, H. *et al.* Magnetite-loaded polymeric micelles as ultrasensitive magnetic-resonance probes. *Adv. Mater.* **17**, 1949–1952 (2005).
73. Liu, S., Guo, S., Sun, S. & You, X. Z. Dumbbell-like Au-Fe3O4 nanoparticles: A new nanostructure for supercapacitors. *Nanoscale* **7**, 4890–4893 (2015).
74. Training workshop and summer school on Magnetic Nanohybrids for cancer therapy. in (2020).
75. Jacobs, B. Optimizing The Surface Chemistry Of Iron Oxide Nanoparticles (Fe 3 O For Colloidal Stability In Hydrophilic Media. (TU Delft, 2020).
76. Natividad, E., Castro, M. & Mediano, A. Accurate measurement of the specific absorption rate using a suitable adiabatic magnetothermal setup. *Appl. Phys. Lett.* **92**, 5–8 (2008).
77. Khurshid, H. *et al.* Anisotropy effects in magnetic hyperthermia: A comparison between spherical and cubic exchange-coupled FeO/Fe3O4 nanoparticles. *J. Appl. Phys.* **117**, 1–5 (2015).

Appendix I

```python
#
# Calculation of Ms, Hc and Mr
#

# Import all necessary libraries
import sys
import numpy as np
import pandas as pd
import matplotlib.pyplot as plt
import os
import glob

# Load raw data of magnetometry measurements
df = pd.ExcelFile('E47_OA,OAm.xlsx').parse('Sheet1') #you could add index_col=0 if there's an index
f=[]
f.append(list(df['Field (Oe)']))

mag=[]
mag.append(list(df['emu/g']))

# Find the x = 0 intersects of SQUID curve and thus coercivity
for x, y in zip(f[0], mag[0]):
    if x == 0:
        print(y)



# Find the y = 0 intersects of SQUID curve and thus remanent magnetization
# An interpolation step was used
f1=[]
mag1=[]
f1.append(f[0][0])
mag1.append(mag[0][0])
for i in range(len(f[0])):
    f1.append(f[0][i])
    mag1.append(mag[0][i])
    if (mag1[-2]>0 and mag1[-1]<0) or (mag1[-2]<0 and mag1[-1]>0):
        mag1.append(0)
        f1.append((f1[-1]+f1[-2])/2)
for x, y in zip(f1, mag1):
    if y == 0:
        print(x)

# Find saturation magnetization
max(mag[0])


#
# Calculation of blocking temperature from ZFC curves
#

# Extract ZFC from ZFC - FC curves
for x, y in zip(temp[0], mag[0]):
    if x == max(temp[0]):
        maxy = y

index = mag[0].index(maxy)

m2 = []
for i in range(len(mag[0])):
    if i < index:
        m2.append(mag[0][i])

```

```
t2 = []
for i in range(len(temp[0])):
    if i < index:
        t2.append(temp[0][i])

# Find temperature that corresponds to the maximum of ZFC curve
for a, b in zip(t2, m2):
    if b == max(m2):
        max_temp = a

max_temp
```

```
#
# SLP calculation using the ISM
#

import sys
import numpy as np
import pandas as pd
import matplotlib.pyplot as plt
import os
import glob

#Setting the parameters for SAR calculation
def calculate_sar(filename):
    volume_sample   = 1     #volume of the sample solution in mL
    density_s       = 0.672 #density of solvent in g/mL, for water take 1, for hexane 0.672
    np_conc         = 5.2   #concentration of magnetic nanoparticles in mg/ml
    spec_heat       = 2.26  #specific heat for colloid. For small concentrations same
                            #as the solvent. For water = 4.181 J/g/K, for hexane 2.26 J/g/K
    m_s = density_s * volume_sample            #mass of solvent in g
    m_n = np_conc * volume_sample * 0.001      #mass of nanoparticles in g
    Cp = spec_heat * (m_s + m_n)               #Specific heat of total sample

    #import data as pandas dataframe
    data = pd.read_csv(filename, header=0,)

    #search for the time the magnetic field is turned on

    time_field_on = int(data[data.status == "AMF_ON"].head(1).seconds)

    #then select a time interval for delta_temperature
    #for now interval taken is 5 sec after AMF_ON to 15 sec after AMF_ON

    delta_temp = (data.loc[time_field_on + 15, 'temp_channel_A'] - data.loc[time_field_on + 5, 'temp_channel_A'])*0.1

    if delta_temp <= 0:
        print('Processing ' + filename + ' gave an error:')
        print('Error: delta temperature is zero or negative, namely ' + str(delta_temp))
        sys.exit()

    print('Delta temperature found is ' + str(np.round(delta_temp,4)) + ' degrees Celsius per second')

    #After finding the delta temperature, the SAR value is calculated
    #for the formula used see https://iopscience.iop.org/article/10.1088/1361-6463/ab140c
    #in short, SAR = (m_s / m_n) * Cp * delta_temp with m_s is mass of solvent,
    #m_n is mass of nanoparticles, and Cp is specific heat of colloid

    SAR = (m_s / m_n) * Cp * delta_temp

    #determine used frequency and field strenght

```

```
    frequency = data.frequency[1]/1000
    field_strenght = data.mT[time_field_on]

    print('SAR value calculated is ' + str(np.round(SAR,2)) + ' W/g')

    # determine the temperature increase during AMF exposure

    temp1 = data[data.status == "AMF_ON"].temp_channel_A.iloc[0]   #temperature at the moment when AMF is turned on
    temp2 = data[data.status == "AFTER"].temp_channel_A.iloc[0]    #temperature at the moment when AMF is switched off
    temp_increase = temp2 - temp1                                  #temperature increase

    print('The temperature before exposure was ' + str(np.round(temp1,2)) + ' degrees Celsius')
    print('The maximum temperature reached was ' + str(np.round(temp2,2)) + ' degrees Celsius')
    print('The temperature increased ' + str(np.round(temp_increase,2)) + ' degrees Celsius in one minute of exposure')

    # plot temperature over time

    tempA = data.temp_channel_A   #temperature at the centre of the vessel
    tempB = data.temp_channel_B   #temperature at the side and bottom of the vessel
    time = data.seconds/60

    plt.plot(time,tempA, '-r', label='T center')
    plt.plot(time,tempB, '-g', label='T side and bottom')
    plt.legend(loc='upper left')
    plt.ylabel("Temperature (Celsius)")
    plt.xlabel("Time (min)")
    plt.title("Temperature over time")

    results1 = [frequency, field_strenght, temp1, temp2, temp_increase, SAR]
    results = [round(num,2) for num in results1]
    #headers = ['Frequency (kHz)', 'Magnitute (mT)', 'Initial T (Celsius)', 'Maximum T (Celsius)',
               #'T increase (Celsius)', 'SAR (W/g)']
    #table = pd.DataFrame({'Variables':headers, 'Values':results})
    print(results)

    return SAR, frequency, field_strenght, temp_increase
```

```
#
# Exponential fitting of cooling curve
#

import sys
import numpy as np
import pandas as pd
import matplotlib.pyplot as plt
import os
import glob
from scipy.optimize import curve_fit
import lmfit

#import data as pandas dataframe, load e.g. E68 experiment data
data = pd.read_csv('E68 - 345 kHz - 19 mT - 1m - 1m - 1m - 20 C - 5.2 mg - 1 mL - hexane.csv')
tempA68b =data68.loc[data68['status'] == 'AFTER'].temp_channel_A   #temperature at the centre of the vessel
time68b = data68.loc[data68['status'] == 'AFTER'].seconds
time68 = time68b[(time68b > 125)]    # x data
tempA68 = tempA68b[(time68b > 125)]  # y data

```

```python
# Use lmfit library to fit an exponential model
mod = lmfit.models.ExponentialModel()
pars = mod.guess(tempA68, x=time68)
out = mod.fit(tempA68, pars, x=time68)

print(out.fit_report())
out.plot()
out.values
```

```python
#
# LRT model fitting for frequency and magnitute
#


import numpy, scipy, matplotlib
import matplotlib.pyplot as plt
from scipy.optimize import curve_fit
from scipy.optimize import differential_evolution
import warnings

xData = numpy.array([157, 190, 250, 297])
yData = numpy.array([3.93, 8.72, 13.33, 13.28])

def func(x, a, b, Offset): # Sigmoid A With Offset from zunzun.com
    return (a * ((x**2) / (1.0 + (x**2)))+b) + Offset

# function for genetic algorithm to minimize (sum of squared error)
def sumOfSquaredError(parameterTuple):
    warnings.filterwarnings("ignore") # do not print warnings by genetic algorithm
    val = func(xData, *parameterTuple)
    return numpy.sum((yData - val) ** 2.0)


def generate_Initial_Parameters():
    # min and max used for bounds
    maxX = max(xData)
    minX = min(xData)
    maxY = max(yData)
    minY = min(yData)

    parameterBounds = []
    parameterBounds.append([minX, maxX]) # search bounds for a
    parameterBounds.append([minX, maxX]) # search bounds for b
    parameterBounds.append([0.0, maxY]) # search bounds for Offset

    # "seed" the numpy random number generator for repeatable results
    result = differential_evolution(sumOfSquaredError, parameterBounds, seed=3)
    return result.x

# generate initial parameter values
geneticParameters = generate_Initial_Parameters()

# curve fit the test data
fittedParameters, pcov = curve_fit(func, xData, yData, geneticParameters)

print('Parameters', fittedParameters)

modelPredictions = func(xData, *fittedParameters)

absError = modelPredictions - yData

SE = numpy.square(absError) # squared errors
MSE = numpy.mean(SE) # mean squared errors
RMSE = numpy.sqrt(MSE) # Root Mean Squared Error, RMSE
```

```python
Rsquared = 1.0 - (numpy.var(absError) / numpy.var(yData))
print('RMSE:', RMSE)
print('R-squared:', Rsquared)



##########################################################
# graphics output section
def ModelAndScatterPlot(graphWidth, graphHeight):
    f = plt.figure(figsize=(graphWidth/100.0, graphHeight/100.0), dpi=100)
    axes = f.add_subplot(111)

    # first the raw data as a scatter plot
    axes.plot(xData, yData, 'o', color="green", label = 'Experimental data - Modified Law of Cooling')

    # create data for the fitted equation plot
    xModel = numpy.linspace(min(xData), max(xData))
    yModel = func(xModel, *fittedParameters)

    # now the model as a line plot
    axes.plot(xModel, yModel, '.', color="orange", label = 'LRT SLP')
    axes.plot(xModel, yModel, '.', color="orange", label = 'R-squared: 0.98')

    axes.set_xlabel('Frequency (kHz)') # X axis data label
    axes.set_ylabel('SLP (W/g)') # Y axis data label
    plt.legend(loc='upper left')
    plt.show()
    plt.close('all') # clean up after using pyplot

graphWidth = 800
graphHeight = 600
ModelAndScatterPlot(graphWidth, graphHeight)
```